H2A.Z deposition at meiotic prophase I underlies homologous recombination and pachytene genome activation during male meiosis

Shenfei Sun[1,5,*], Yamei Jiang[1,5], Ning Jiang[1,5], Qiaoli Zhang[1,4], Hongjie Pan[2], Fujing Huang[1], Xinna Zhang[4], Yuxuan Guo[4], Xiaoyu You[1], Kai Gong[1], Wei Wei[1], Hanmin Liu[3], Zhenju Song[1], Yuanlin Song[1], Xiaofang Tang[1], Miao Yu[1], Runsheng Li[2], Xinhua Lin[1,3,6,*]

Affiliations

[1]State Key Laboratory of Genetic Engineering, Greater Bay Area Institute of Precision Medicine (Guangzhou), School of Life Sciences, Zhongshan Hospital, Fudan University, Shanghai, 200438, China;

[2]National Health Commission (NHC) Key Laboratory of Reproduction Regulation, Shanghai Institute for Biomedical and Pharmaceutical Technologies, Shanghai, 200032, China;

[3]The Joint Laboratory for Lung Development and Related Diseases of West China Second University Hospital, Sichuan University and School of Life Sciences of Fudan University, Chengdu, 610041, China;

[4]State Key Laboratory of Reproductive Regulation and Breeding of Grassland Livestock, School of Life Sciences, Inner Mongolia University, Hohhot, 010070, China;

[5]These authors contributed equally to this work;

[6]Lead contact.

[*]Correspondence to: xlin@fudan.edu.cn (X.L.); shenfei_sun@fudan.edu.cn (S.S.).

Keywords: male meiosis; pachytene genome activation; homologous recombination; Znhit1; chromatin remodeling;

Abstract

Accurate meiotic progression is important for gamete formation and the generation of genetic diversity. However, little is known about the identity of chromatin regulators that underlie mammalian meiosis in vivo. Here, we identify the multifaceted functions of the chromatin remodeler Znhit1 in governing meiosis. We observe a gradual increase in *Znhit1* expression during the meiotic prophase. Znhit1 deficiency in spermatocytes results in arrested pachytene development, impaired DNA double-strand break repair, and defective homologous recombination. Single-cell RNA sequencing and transcriptome analysis reveal that Znhit1 loss downregulates the transcription of pachytene genome activation (PGA) genes globally. Chromatin immunoprecipitation data show that Znhit1 is needed for the incorporation of the histone variant H2A.Z into pachytene chromatin. Moreover, we find that H2A.Z cooperates with the transcription factor A-MYB to co-bind DNA elements and control enhancer activity. Our findings provide insights into the regulatory mechanisms governing meiotic progression and highlight Znhit1 as a critical regulator of meiotic recombination and PGA.

Introduction

Meiosis is a fundamental and conserved process that plays a crucial role in gamete formation and the generation of genetic diversity. By undergoing one round of DNA replication and two rounds of cell division, the meiotic process ensures the production of haploid cells, each with a unique combination of genetic materials (Handel and Schimenti, 2010; Lascarez-Lagunas et al., 2020). Any disruptions to the normal progression of meiosis would have significant consequences, such as aneuploidy, infertility, spontaneous abortion, and congenital diseases (Hassold and Hunt, 2001). Therefore, understanding the molecular mechanisms underlying meiosis will provide valuable insights for the diagnosis and treatment of reproductive and developmental diseases.

Multiple chromosomal events occur during meiotic prophase I, including homologous chromosome pairing and synapsis, DNA double-strand break (DSB) formation and repair, and homologous recombination (HR) (Baudat et al., 2013; Hunter, 2015; Zickler and Kleckner, 2023). In this process, homolog pairing and synapsis coincide with Spo11-mediated genome-wide formation of DSBs (Bergerat et al., 1997; Keeney et al., 1997). Following the formation of DSBs, the DNA undergoes resection, leading to the generation of single-stranded DNA overhangs. These overhangs are then coated by RPA, DMC1, and RAD51, facilitating the production of recombination intermediates. Subsequently, these intermediates are processed and resolved, ultimately forming either meiotic crossovers or non-crossovers (Gray and Cohen, 2016; San Filippo et al., 2008; Symington, 2014). The tightly coordinated timing and spatial arrangement of these meiotic events are of utmost importance for proper germ cell development.

There is transcriptional awakening during male meiotic prophase I, in which the quiescent meiotic genome becomes transcriptionally active during the zygotene-to-pachytene transition (Ernst et al., 2019; Green et al., 2018; Rabbani et al., 2022; Turner, 2015). This process, referred to as pachytene genome activation (PGA), is responsible for the expression of numerous genes and plays an essential role in controlling meiotic and post-meiotic events. Previous studies have emphasized the significance of the transcription factors (TFs) A-MYB, BRDT, and TCFL5 in activating transcription during pachytene (Alexander et al., 2023; Bolcun-Filas et al., 2011; Cecchini et al., 2023; Gaucher et al., 2012; Li et al., 2013; Maezawa et al., 2020; Manterola et al., 2018; Ozata et al., 2020; Yu et al., 2021). Additionally, extensive chromatin remodeling takes place in spermatocytes during meiotic prophase I, involving histone variant exchange, histone modifications, and high-order genome rearrangement (Kota and Feil, 2010; Wang et al.,

2017; Zheng and Xie, 2019). It has been known that SETDB1-mediated H3K9 trimethylation (H3K9me3) is required for sex chromosome transcription silencing (a process called meiotic sex chromosome inactivation, MSCI) and male meiotic procession (Hirota et al., 2018). However, the specific involvement of chromatin regulators in gene activation on autosomes remains poorly understood.

Zinc finger HIT-type containing 1 (Znhit1), an evolutionarily conserved subunit of the SRCAP chromatin remodeling complex, acts as a key regulator for the histone variant H2A.Z deposition to control gene expression and cell fate determination (Cai et al., 2005; Cuadrado et al., 2007; Feng et al., 2022). Recent studies have shown that Znhit1 is involved in a wide range of developmental processes, including muscle and lens differentiation, heart development, lung branching, and adult tissue stem cell maintenance (Cuadrado et al., 2010; Lu et al., 2022; Sun et al., 2020; Wei et al., 2022; Xu et al., 2021; Zhao et al., 2019). In our most recent study, we deleted Znhit1 in early male germ cells and found that Znhit1 is required for the mitosis-to-meiosis transition by controlling Meiosin expression (Sun et al., 2022). However, the in vivo function of Znhit1 in regulating meiotic progression remains unknown.

To delve into the function of Znhit1 in meiosis, we analyzed Znhit1 expression and observed upregulated Znhit1 expression specifically during meiotic prophase. Here, we examine the role of Znhit1 in multiple meiotic events and show that the deletion of Znhit1 in spermatocytes causes impaired HR and defective PGA, thereby resulting in meiotic developmental arrest. Hence, our study highlights the essential role of Znhit1 in ensuring meiotic progression, implicating its potential as a therapeutic target for meiosis-related diseases.

Results

Znhit1 expression is upregulated during meiotic prophase and *Znhit1* knockout in spermatocytes disrupts spermatogenesis

To identify potential chromatin regulators in meiosis, we first queried for chromatin factors highly expressed during the zygotene stage based on published transcription data (Fig S1A and Table S1) (Chen et al., 2018). Quantitative analysis showed that the chromatin remodeler Znhit1 was among the most highly expressed factors (Figs 1A, 1B, S1B, and S1C). RNA in situ hybridization validated that *Znhit1* expression in male germ cells decreased after meiotic initiation, followed by a gradual increase in spermatocytes from the zygotene stage to the metaphase stage (Fig 1C). These results suggest that Znhit1 is a potential chromatin regulator of meiotic progression.

To investigate whether Znhit1 regulates meiotic progression, we generated spermatocyte-specific *Znhit1* knockout mice (*Znhit1*$^{fl/fl}$; *Stra8-cre*, referred to as *Znhit1*-sKO). In the first wave of spermatogenesis, Ngn3-negative prospermatogonia directly differentiate into A2 spermatogonia(Law et al., 2019; Rabbani et al., 2022; Yoshida et al., 2006; Yoshida et al., 2004). With Stra8-cre inducing recombination in A1 spermatogonia and preleptotene spermatocytes separately(Lin et al., 2017), it is feasible to generate mice with spermatocyte-specific gene knockout (Fig 1D). RNA in situ experiments on testis sections confirmed *Znhit1* mRNA deletion in spermatocytes (Figs 1E and S1D). Compared with littermate controls, *Znhit1*-sKO male mice had smaller testes (Fig S1E and S1F). PAS-histological and PNA-fluorescence staining illuminated the absence of round spermatids and elongated spermatids in *Znhit1*-sKO testes (Fig 1F and 1G), indicating that *Znhit1* knockout in spermatocytes disrupted spermatogenesis.

Znhit1 deletion leads to meiotic arrest at the pachytene stage

To dissect spermatocyte development in *Znhit1*-sKO testes, we co-stained SYCP3, a marker of primary spermatocytes, and HSPA2, a testis-specific HSP70 family member that accumulates from the pachytene stage onward. As shown in Figure 2A, both control and *Znhit1*-sKO testis sections exhibited SYCP3^{+}HSPA2^{+} primary spermatocytes. Phospho-histone H3 (Thr3) (pH3) is a marker of mitotic and meiotic metaphase cells, and Znhit1 deletion caused the complete absence of pH3^{+} metaphase spermatocytes within the cavity of seminiferous tubules (Fig 2B). These results suggest that Znhit1 deletion causes spermatocyte arrest at meiotic prophase I.

To pinpoint the onset of meiotic failure, we performed immunostaining against SYCP3 in spermatocyte chromosome spreads. The wild-type testes displayed typical spermatocytes at consecutive substages, including leptotene, zygotene, pachytene, diplotene, and diakinesis (Fig 2C). However, spermatocytes at the diplotene and diakinesis stages were rarely observed in *Znhit1*-sKO testes (Fig 2D and 2E). We also examined the expression of H1T, a middle pachytene marker, and no difference in H1T expression was observed in *Znhit1*$^{-/-}$ spermatocytes (Fig S2A). Moreover, *Znhit1* knockout resulted in increased TUNEL-positive spermatocytes, suggesting that these defective spermatocytes were eliminated by the apoptotic pathway (Fig 2F and 2G). These results indicate that Znhit1 deletion leads to meiotic arrest at the pachytene stage.

Znhit1 is required for DSB repair and meiotic recombination

To investigate the impact of Znhit1 on meiotic events, we first performed immunostaining of SYCP1 and SYCP3, the essential components of the synaptonemal complex, to examine whether Znhit1 regulated homologous synapses. As shown in Figure 3A, pachytene nuclei with fully synapsed autosomes were observed in spermatocytes from control and *Znhit1*-sKO testes. During the pachytene stage, the X and Y chromosomes undergo pairing and synapses between the short pseudoautosomal regions (PARs). We found an increase in the percentage of unsynapsed X-Y chromosomes in *Znhit1*-sKO spermatocytes (Fig 3B). Thus, deletion of Znhit1 results in impaired sex chromosomal synapsis.

Next, we examined the programmed formation and repair of DSBs by co-staining SYCP3 and γH2AX, a DSB marker, on spermatocyte chromosome spreads. In both control and *Znhit1*-sKO spermatocytes, γH2AX signals were evident in the leptotene and zygotene stages (Fig 3C). However, in Znhit1-deficient pachynema, we still observed diffuse γH2AX signals on the autosomes, while in control pachynema, γH2AX signals only accumulated on the X-Y chromosomes. Moreover, we detected the presence of another DSB marker, phospho-ATM (pATM), on the autosomes in *Znhit1*-sKO pachytene spermatocytes (Fig 3D). Together, these results demonstrate that Znhit1 is required for completing DSB repair.

To understand how Znhit1 regulates DSB repair, we performed an immunostaining analysis using the markers RPA2 and DMC1, the essential factors involved in DSB repair by coating resected DSBs. We found an increase in RPA2 and DMC1 counts in both

zygonema and pachynema of *Znhit1*-deficient testes (Fig 3E, 3F, and S3A), indicating that Znhit1 deletion delayed recombinational repair, resulting in defective resolution of autosomal DSBs in *Znhit1*$^{-/-}$ pachynema. The formation and repair of DSBs play crucial roles in initiating and facilitating meiotic recombination, respectively. To examine the consequences of unrepaired DSBs on meiotic recombination in Znhit1 mutants, we performed an immunostaining analysis against MLH1, a marker of meiotic crossover formation. Indeed, we found an almost absence of MLH1 foci in *Znhit1*$^{-/-}$ pachytene spermatocytes compared with controls (Fig 3G and 3H), indicating that the loss of Znhit1 severely disrupted meiotic crossover formation.

Collectively, these results argue that Znhit1 is essential for multiple meiotic events, including sexual chromosome synapsis, DSB repair, and homologous recombination.

scRNA-seq analysis reveals abnormal pachytene-to-diplotene transition caused by *Znhit1* knockout

We then asked how Znhit1 regulates spermatocyte development. We isolated testicular cells from control and *Znhit1*-sKO mice at postnatal 16 (P16) and performed scRNA-seq analysis. After quality control, a total of 2,4164 cells (12,212 cells from control, 11,952 cells from *Znhit1*-sKO) were captured, yielding 2,473 genes per cell. As visualized via uniform manifold approximation and projection (UMAP), the single-cell atlas comprised germ cells at various stages and major somatic cell types, including Sertoli cells (*Sox9*$^{+}$), Leydig cells (*Hsd3b1*$^{+}$), peritubular myoid cells (*Acta2*$^{+}$), and macrophages (*Adgre1*$^{+}$) (Figs 4A, 4B and S4A, and Table S2). The scRNA-seq data identified 6 germ cell types based on the expression of specific markers, including undifferentiated spermatogonia (*Zbtb16*$^{+}$), differentiating spermatogonia (*Kit*$^{+}$), preleptotene spermatocytes (*Nacad*$^{+}$), leptotene spermatocytes (*Meiob*$^{+}$), zygotene spermatocytes (*Gml*$^{+}$), and pachytene spermatocytes (*Ldhc*$^{+}$) (Fig 4B and 4C). Examination of germ cell scRNA-seq profiles via unsupervised clustering revealed decreased pachytene spermatocytes after *Znhit1* deletion (Figs 4D, 4E, and S4B). *Pou5f2* is expressed explicitly at the diplotene stage, and we found a lack of *Pou5f2*$^{+}$ diplotene spermatocytes in *Znhit1*-sKO testes (Fig 4F). These results indicate that Znhit1 is required for male germ cell development beyond the pachytene stage.

Znhit1 deletion impairs meiotic transcriptional activation

Next, we asked whether meiotic transcriptional activation was affected by Znhit1 deletion. We analyzed changes in gene expression between consecutive spermatocyte stages and identified 4,603 genes that showed significant changes (Fig 5A and Table S3). Of the changed genes between zygotene spermatocytes and pachytene spermatocytes, 1,560 genes were upregulated (referred to as pachytene-activated genes or PGA genes). Moreover, we identified differentially expressed genes (DEGs) in each spermatocyte type between the control and *Znhit1*-sKO groups. The number of DEGs gradually increased from the preleptotene stage to the pachytene stage, with downregulated genes being predominant (Fig 5B and Table S4). In particular, *Znhit1*$^{-/-}$ pachytene spermatocytes exhibited 2,785 downregulated genes, among which were most of the pachytene-activated genes (1,094 out of 1,560, 70.1%; Figs 5B-5D, and S5A). Gene Ontology (GO) enrichment analysis revealed that upregulated genes following Znhit1 deletion were associated with apoptotic pathways, supporting an observation that Znhit1 deletion resulted in germ cell clearance through apoptosis. Moreover, downregulated GO terms included germ cell development and DNA recombination (Fig 5E and Table S5). Interestingly, recent studies showed that cilium organization was essential for spermatocyte development (Mytlis et al., 2022), and Znhit1 deletion reduced the expression of cilium-related genes in zygotene and pachytene spermatocytes (Fig 5E).

We further conducted bulk RNA-seq experiments with P14 control and *Znhit1*-sKO testicular cells and identified 882 DEGs (812 downregulated genes and 70 upregulated genes) in *Znhit1*-sKO testicular cells (Figs 5F and S6A, and Table S6). Through integrative analysis of bulk and single-cell RNA-seq data, we found that the expression of these 812 genes was activated during the zygotene-to-pachytene transition and Znhit1 deletion significantly reduced the expression of these genes (Figs 5G, 5H, and S5B). The downregulated genes following Znhit1 loss were enriched for germ cell-related GO terms, such as cilium formation and spermatid development (Fig S6B). Together, these data argue that Znhit1 is required for meiotic transcriptional activation.

Consistent with meiotic recombination defects in Znhit1 mutants, gene set enrichment analysis (GSEA) revealed that the expression of HR-related genes was globally downregulated following Znhit1 loss (Fig 5I and Table S7). The top genes associated with this function included *Ccnb1ip1*, *Rnf212*, *Spo16*, *Ankrd31*, and *Terb1* (Boekhout et al., 2019; Papanikos et al., 2019; Qiao et al., 2014; Rao et al., 2017; Reynolds et al., 2013; Shibuya et al., 2014; Wang et al., 2019; Zhang et al., 2019) (Figs 5J, S6C, and S6D). As

expected, the Rnf212-dependent sumoylation level decreased in *Znhit1*$^{-/-}$ spermatocytes (Fig 5K). These results suggest that Znhit1 regulates meiotic recombination by activating HR-related genes.

Znhit1 deletion impairs H2A.Z incorporation into pachytene chromatin

We then asked how Znhit1 regulates transcription. Znhit1 is a subunit of the SRCAP complex that facilitates the incorporation of the histone variant H2A.Z by replacing H2A (Fig S7A). Immunostaining against H2A.Z showed a gradual increase in H2A.Z accumulation on autosomes from the leptotene to the diakinesis stage, while the H2A.Z signal was markedly low on the X-Y body (Fig 6A). Znhit1 loss decreased H2A.Z staining on the pachytene cells, suggesting that Znhit1 is required for maintaining H2A.Z integrity during meiosis.

To probe the H2A.Z targets, we performed chromatin immunoprecipitation followed by sequencing (ChIP-seq) against H2A.Z in P14 testicular cells. Using the ChromHMM model to annotate H2A.Z signals with meiocyte chromatin states defined by published epigenetic markers (Spruce et al., 2020), we found that H2A.Z sites were primarily enriched in chromatin state 1 and state 2 (promoters and enhancers) but were less enriched in recombination hotspots (Fig 6B and 6C), consistent with previously published results (Spruce et al., 2020). Quantitative analysis showed significant H2A.Z binding reduction at 37.9% (23,926 of 63,109) of H2A.Z-bound genome sites following Znhit1 deletion (Fig 6D). Comparison analysis with bulk RNA-seq data identified 480 downregulated DEGs with decreased H2A.Z signals (Fig 6E). ~41.3 and 37.8% of the downregulated H2A.Z peaks occupied promoters and enhancers, respectively. At promoters, these downregulated H2A.Z preferentially occupied active promoters (H3K4me3 only), while H2A.Z occupied three types of enhancers: active, poised, and primed enhancers (Figs 6F, S7B, and S7C). These findings indicate that Znhit1 deletion impairs H2A.Z incorporation into pachytene chromatin.

H2A.Z deposition cooperates with A-MYB to regulate transcription

We further asked how Znhit1/H2A.Z deposition facilitates lineage-specific gene expression. We performed TF motif analysis using active promoters/enhancers with decreased H2A.Z signals. This analysis identified several MYB family TFs, including MYB, A-MYB, and B-MYB (Fig 7A). Transcriptional network analysis conducted by

SCENIC further identified A-MYB (encoded by *Mybl1* gene) as the core regulatory TF in spermatocytes (Fig 7B). We reanalyzed RNA-seq data in P14 testes from A-MYB-deficient mice (Li et al., 2013) and found that A-MYB-deficient DEGs correlated with those observed in Znhit1-deficient testicular cells (Fig 7C). Although Znhit1 deletion didn't affect *Mybl1* mRNA expression, transcriptome analyses showed that the expression of A-MYB target genes was significantly reduced in *Znhit1*$^{-/-}$ pachytene spermatocytes (Figs 7D, 7E, S8A, and S8B). These results suggest that *Znhit1*$^{-/-}$ and *Mybl1*$^{-/-}$ pachytene spermatocytes share common gene expression alterations.

Next, we compared the genome binding sites of H2A.Z and A-MYB. Utilizing published A-MYB ChIP-seq data from P14 testicular cells (Li et al., 2013), we identified 6,088 A-MYB binding signals, with 78.1% (4755) of these coinciding with H2A.Z peaks (Fig 7F). Annotation of genomic features showed that approximately 66.52% and 12.02% of these overlapping sites occupied active promoters and enhancers, respectively, representing a stronger enrichment compared to other regulatory elements (Fig 7G). Genes associated with H2A.Z and A-MYB binding included essential HR-related genes, such as *Ccnb1ip1* (encode the Hei10 protein) (Fig 7H). Moreover, we showed that Znhit1 deletion resulted in a marked reduction in H2A.Z signals and nascent transcription identified by KAS-seq signals (Fig 7I and 7J).

Previous studies have shown the fundamental role of A-MYB in activating meiotic enhancers (Maezawa et al., 2020). Enhancer activity is linked to an increased formation of enhancer single-stranded DNA (ssDNA), which can be evaluated using KAS-seq (Wu et al., 2020). We found that the removal of Znhit1 resulted in abolished ssDNA at active enhancers (Fig 7I and 7J). Interestingly, the chromatin accessibility detected by ATAC-seq at active enhancers increased after Znhit1 deletion. These findings suggest that Znhit1/H2A.Z deposition is essential for enhancer activation.

Together, these results demonstrate the critical role of the Znhit1/H2A.Z/A-MYB axis in governing transcriptional activation and enhancer activity.

Discussion

Meiosis plays a crucial role in the production of haploid gametes. Any disturbances during meiotic progress are known to lead to infertility and congenital diseases. Here we delineate the multifaceted functions of the chromatin remodeler Znhit1 in regulating meiotic progression. Our study provides convincing data to show that the Znhit1/H2A.Z/A-MYB axis controls spermatocyte development, meiotic recombination, and PGA. Thus, these findings underscore the significance of specific chromatin structures in governing appropriate transcriptional reprogramming and precise meiotic recombination.

The role of H2A.Z in DNA injury and repair has been extensively studied (Colino-Sanguino et al., 2022; Dong et al., 2014; Xu et al., 2012; Yamada et al., 2018), but its function in programmed DSB formation and repair during mammalian meiosis remains unknown. To address this question, we generated Znhit1 conditional knockout mice specifically during male meiosis to examine the role of Znhit1-mediated H2A.Z deposition in the formation and repair of programmed DSB. One new observation in this study is that Znhit1 loss is dispensable for DSB formation but necessary for DNA break repair during meiosis. Intriguingly, unlike the observations in plant meiosis, we found that H2A.Z does not directly bind DNA recombination sites in mammalian spermatocytes (Choi et al., 2013; Spruce et al., 2020; Wang and Copenhaver, 2018). Moreover, we showed that Znhit1 deletion delays recombinational repair, but has limited impacts on DNA resection, ultimately causing defective meiotic crossover formation. Importantly, our study demonstrates that Znhit1 is essential for the expression of meiotic recombination-related genes, such as *Ccnb1ip1* and *Rnf212*, implying that Znhit1/H2A.Z modulates meiotic recombination through transcriptional regulation. Therefore, our data reveals a different mechanism underlying meiotic recombination between plants and mammals.

Pachytene spermatocytes utilize a highly specific mechanism of meiotic surveillance, the pachytene checkpoint, to prevent aneuploidy formation by removing abnormal germ cells with incomplete chromosome synapsis and defective homologous recombination (Huang and Roig, 2023; Roeder and Bailis, 2000; Subramanian and Hochwagen, 2014). Two checkpoint pathways exist in male meiosis: one responding to unrepaired DSBs and the other triggered by MSCI failure (Royo et al., 2013). However, whether epigenetic regulation is involved in meiotic surveillance is not well defined. Previous studies have

reported that upon stimulation by unrepaired DSBs, the MRE11-ATM-CHK2 pathway is activated to eliminate aberrant germ cells (Marcet-Ortega et al., 2017). Our study found that Znhit1 deletion impairs the removal of ATM phosphorylation signals on autosomes in pachynema, ultimately causing meiotic pachytene arrest and apoptosis. Therefore, these findings demonstrate that Znhit1 acts as an important chromatin factor involved in the regulation of the pachytene checkpoint.

It has long been noticed that in meiotic prophase I, chromatin that has not yet completed chromosomal synapses is transcriptionally inactive, known as meiotic silencing of unsynapsed chromatin (MSUC) (Turner et al., 2005). When germ cells enter the pachytene stage, a large number of protein-coding genes and non-coding RNAs begin to be actively expressed, known as PGA. Previous studies have shown that transcription factors A-MYB and BRDT are involved in transcriptional activation during meiotic prophase, but how PGA takes place in the chromatin context is unclear. In this study, we found that the expression of the chromatin remodeler Znhit1 is specifically upregulated during the zygotene-to-pachytene transition. We also observed that H2A.Z deposition is enriched in the autosomes but less in the sex chromosome at the pachytene stage. Znhit1 deletion in spermatocytes repressed pachytene gene activation globally and reduced chromosome-wide H2A.Z deposition, supporting a central role of Znhti1 in PGA regulation and chromatin remodeling. It has been known that A-MYB is a transcription factor that controls pachytene transcription activation. We found that Znhit1-deficient spermatocytes phenocopied abnormal meiotic phenotypes in A-MYB mutants, such as X-Y synapsis failure, impaired DSB repair, and defective HR (Alexander et al., 2023; Bolcun-Filas et al., 2011; Li et al., 2013; Maezawa et al., 2020). Our results also revealed that Znhit1/H2A.Z cooperates with A-MYB to regulate PGA gene activation. Therefore, our study illuminates the molecular mechanisms underlying the fundamental question of how PGA is regulated.

The histone variant H2A.Z is enriched at gene promoters and regulatory regions, but there is ongoing debate regarding its involvement in transcriptional regulation. A recent paper reported that H2A.Z knockout in post-mitotic muscle cells has limited effects on gene expression (Belotti et al., 2020). In this study, we utilized the meiotic prophase as a model system (where DNA replication does not occur) to study H2A.Z's function in transcriptional regulation. We found that Znhit1-mediated H2A.Z deposition, independent of DNA replication, is indispensable for the transcriptional activation of a large number

of meiotic genes. One explanation of this conflicting phenomenon is that H2A.Z dynamics but not stable H2A.Z accumulation is essential for priming transcriptional changes.

Through the integration of functional and molecular evidence, our findings establish the critical involvement of Znhit1-dependent chromatin remodeling in the orchestration of meiotic progression and coordination of various meiotic processes, such as HR and PGA. Furthermore, we pinpoint the pivotal role played by the Znhit1/H2A.Z/A-MYB axis in driving transcriptional reprogramming during meiotic prophase. Taken together, this study deepens our understanding of the interplay between epigenetic regulation and mammalian meiosis.

Materials and Methods

Animals. *Znhit1*$^{fl/fl}$ mice have been previously described (Zhao et al., 2019) and are available from the Model Animal Research Center of Nanjing University (MARC, Nanjing, China). The *Stra8-cre* knock-in mouse line was kindly provided by Dr. Ming-Han Tong(Lin et al., 2017). All mice were maintained on the C57BL/6J background. Germ cell-specific *Znhit1* knockout mice (*Znhit1*$^{fl/fl}$; *Stra8-cre*) were obtained by crossing *Znhit1*$^{fl/+}$; *Stra8-cre* mice with *Znhit1*$^{fl/fl}$ mice. All mice were housed in the SPF (Specific-Pathogen-Free) animal facility with standard 12 h light/dark cycles and standard temperature (22 to 24°C). All mice were provided with ad libitum access to standard laboratory food and water. All experiments in this study were performed following relevant guidelines and approved by the Animal Care and Use Committee of Fudan University.

Histological and immunohistochemical analysis. Testes were fixed in modified Davidson's fixative as previously described (Latendresse et al., 2002), embedded in paraffin, and sectioned. For periodic acid-Schiff (PAS)-hematoxylin staining, 5 μm testis sections were deparaffinized, rehydrated, and stained with Schiff's reagent and hematoxylin solution. For immunofluorescent staining, 5 μm testis sections were retrieved by sodium citrate antigen retrieval buffer (pH 6.0) and blocked with 5% BSA in PBS for 30 min at room temperature. The sections were later incubated overnight at 4°C with primary antibodies as follows: mouse anti-SYCP3 (Abcam, ab97672), rabbit anti-HSPA2 (Abcam, ab108416), rabbit anti-pH3 (Millipore, H0412), rabbit anti-H1T (Invitrogen, PA5-51200), or lectin PNA (Sigma–Aldrich, L7381). On the following day, secondary fluorescein-conjugated antibodies and DAPI (Sigma–Aldrich, D9542) were added for 1 h, followed by Fluoromount-G mounting (Southern Biotech, 0100-01). Images were analyzed using the confocal microscope.

TUNEL staining was carried out using the DeadEnd^{TM} Fluorometric TUNEL System (Promega, G3250) according to the manufacturer's instructions.

Immunostaining of spermatocyte chromosome spreads. Spermatocyte chromosome spreads were prepared as previously described (Alavattam et al., 2018). Briefly, the clumps of seminiferous tubules were transferred to the hypotonic extraction buffer (30 mM Tris base, 17 mM trisodium citrate, 5 mM EDTA, 50 mM sucrose, 5 mM dithiothreitol (DTT), and 1× protease inhibitor, pH 8.2) and incubated on ice for 1.5 h. The clumps of tubules were then transferred to 30 μL of ice-cold 100 mM sucrose and mashed gently using tweezers to obtain a cell suspension. An additional 30 μL of ice-cold 100 mM sucrose was added to the cell suspension and mixed several times. Positively charged slides were incubated in the ice-cold fixation solution (2% paraformaldehyde, 0.1% Triton X-100, and 0.02% SDS, pH 9.2) for 3 min. 30 μL of the diluted cell suspension was applied to the slides and incubated in humid chambers at room temperature for 2 h. The slides were washed with 0.4% Photo-Flo 200 and stored at -80°C.

For immunostaining of spermatocyte chromosome spreads, slides were washed with PBS and blocked with 5% BSA in PBS for 30 min at room temperature. The slides were stained with primary antibodies as follows: rabbit anti-SYCP3 (Abcam, ab15093), mouse anti-SYCP3 (Abcam, ab97672), rabbit anti-SYCP1 (Abcam, ab15090), mouse anti-γH2AX (BioLegend, 613401), rabbit anti-pATM (Millipore, 05-740), rabbit anti-RAD51 (Proteintech), rabbit anti-RPA2 (Proteintech, 10412-1-AP), rabbit anti-MLH1 (Cell Signaling Technology, 3515T), rabbit anti-H2A.Z (Abcam, ab4174).

***Znhit1* in situ hybridization.** Testis sections (5 μM) at the indicated times were prepared for *Znhit1* in situ hybridization with the RNAscope kit (Advanced Cell Diagnostics, 323100) according to the manufacturer's instructions.

Quantitative reverse transcription PCR (RT-qPCR). Total RNA was isolated using the RNeasy Mini-plus Kit (Qiagen, 74134) and then reverse-transcribed into complementary DNA (cDNA) with the GoScript Reverse Transcription System (Promega, A5003). cDNA was used as the template for the quantitative PCR assay using 2×SYBR Green qPCR Master Mix (Bimake, B21202). Quantitative PCR primers are listed in Table S8.

RNA-seq library generation and sequencing. Total RNA from fresh testes was isolated and mRNA was purified with magnetic beads (Vazyme, N401-01). Then, mRNA was fragmented and processed to generate RNA-seq libraries (Vazyme, NR605-01). Over 40 million reads were obtained per sample using the Illumina NovaSeq platform for 2 independent biological replicates.

Single-cell RNA sequencing (scRNA-seq). P16 control and *Znhit1*-sKO testes were digested by collagenase IV and trypsin at 37°C for 10 min to obtain testicular cell suspensions. scRNA-seq libraries were constructed using a 10 × Genomics kit and sequenced on the Illumina platform.

ChIP-seq library generation and sequencing. ChIP-seq library generation was performed as previously described. Briefly, P14 control and *Znhit1*-sKO testes were digested by collagenase IV and trypsin at 37°C for 10 min, crosslinked with 1% formaldehyde for 10 min, and quenched with glycine. The cells were lysed and sheared with a Bioruptor Plus machine for 20 min. Then, 2 μg of anti-H2A.Z antibody (Abcam, ab4174) was added to the sonicated chromatin and incubated overnight at 4°C. The following day, 20 μL of protein G beads were added and incubated for 2 h at 4°C. The beads were washed and reverse-crosslinked for 4 h at 65°C. DNA was extracted using phenol-chloroform and subjected to library construction using the VAHTS Universal DNA Library Prep Kit for Illumina (Vazyme, ND607-01) according to the manufacturer's instructions. Over 30 million reads were obtained per sample using the Illumina NovaSeq platform for 2 independent biological replicates.

KAS-seq library and ATAC-seq library generation and sequencing. Testes were digested by collagenase IV and trypsin at 37°C for 10 min. Pachytene cells were sorted using fluorescence-activated cell sorting (FACS) as previously described (Long et al., 2017). For KAS-seq, pachytene cells were labeled with N3-kethoxal, and DNA was isolated using the DNA Clean and Concentrator kit (Zymo, D4013) and subjected to library construction using Q5 high-fidelity DNA polymerase (New England Biolabs, M0544S). Genomic DNA was fragmented using Tn5 transposase and subjected to library

construction. For ATAC-seq, pachytene nuclei were isolated and fragmented with Tn5 transposase. DNA was isolated using the DNA Clean and Concentrator kit (Zymo, D4013) and subjected to library construction using Q5 high-fidelity DNA polymerase (New England Biolabs, M0544S). For high-throughput sequencing, over 30 million reads were obtained per sample using the Illumina NovaSeq platform for 2 independent biological replicates.

RNA-seq data analysis. We performed RNA-seq analysis as described previously (Pertea et al., 2016). Briefly, after removing adapters using Cutadapt (v2.5) (Kechin et al., 2017), paired-end reads were aligned to the annotated mouse transcripts (mm10 Gencode vM23 release) using Hisat2 (v2.2.1) (Kim et al., 2015; Kim et al., 2019). Gene expression levels were calculated using StringTie (v2.2.1) (Pertea et al., 2015). Read counts were calculated using a Python script (prepDE.py3) provided by the StringTie development team. Differentially expressed genes were identified using the R package DESeq2 (v1.38.3) (Love et al., 2014). Genes with read counts > 50 in at least one sample were kept for further analysis. A given gene was considered to significantly change if the adjusted P value (padj) was < 0.05, the P value was < 0.01, and the fold-change was≥ 2. Gene Set Enrichment Analysis (GSEA) was carried out using GSEA software (Subramanian et al., 2005). GO analysis was performed using clusterProfiler (v4.6.2) (Wu et al., 2021).

scRNA-seq data analysis. FASTQ files were run through CellRanger (v7.1.0) software with default parameters for de-multiplexing, aligning reads with STAR software to mm10, and counting unique molecular identifiers (UMIs). As input files of the Seurat R package (v4.4.0), the filtered gene expression matrices were then used for downstream analyses (Butler et al., 2018). Low-quality cells were filtered (expressing < 500 or >6,000 unique gene counts and >15% mitochondrial reads). Principal component analysis was performed on SCT-transformed data using 3,000 variable genes. The top 50 principal components were used for clustering and visualized using the UMAP algorithm in the Seurat R package. The "FindAllMarkers" function of the Seurat R package was used to calculate

cluster-specific genes. Marker genes for each cluster are shown in Table S2.

The "FindMarkers" function of the Seurat R package was used to identify differentially expressed genes (DEGs) for spermatocytes (preleptotene, leptotene, zygotene, and pachytene). Only those with |'avg_logFC'| > 0.25 and 'p_val_adj' < 0.05 were considered as DEGs. For the transcriptional regulatory network analysis, the raw count matrix was used by the pyscenic (v0.12.1) workflow using default parameters (Aibar et al., 2017). Then, the output loom file was opened by the SCENIC R package (v1.3.1), and AUC values of regulons were extracted for visualization of downstream transcription factor activity.

ChIP-seq and KAS-seq data analysis. For analyzing ChIP-seq and KAS-seq data, we used the ENCODE ChIP-seq pipeline (v2.2.1, https://github.com/ENCODE-DCC/chip-seq-pipeline2). Raw reads were cleaned by Cutadapt (v2.5) (Kechin et al., 2017). After removing adapters, clean reads were aligned against the mouse mm10 genome using bwa (v0.7.17) (Li and Durbin, 2009). Then, sam files were converted to bam files using samtools (v1.9) (Li et al., 2009). PCR duplicates were removed using Picard (v2.20.7) (https://broadinstitute.github.io/picard/). Histone ChIP-seq peaks (such as H2A.Z and histone marks) and KAS-seq peaks were called using MACS2 (v2.2.4) (Zhang et al., 2008), while transcription factor ChIP-seq peaks (such as A-Myb) were called using the R packages spp (v1.15.5) (https://github.com/hms-dbmi/spp). The conservative narrow peaks were used for downstream analysis.

For visualization, bam files were converted to bigWig files using deepTools (v3.3.1) (Ramirez et al., 2014), and bigWig files were used to calculate tag density under 50 bp resolution. In addition, CPM was used to normalize the number of reads per bin. We used the R package DiffBind (v3.8.4) (http://bioconductor.org/packages/release/bioc/html/DiffBind.html) for differential peak analysis and the R package rGREAT (v2.1.11) (Gu and Hubschmann, 2023) for peak annotation. We used ComputeMatrix and plotHeatmap of deepTools to generate count

matrices and heatmaps, respectively. H2A.Z enrichment within chromatin states was annotated using the ChromHMM model (Ernst and Kellis, 2012; Spruce et al., 2020). TF motif enrichment was calculated using HOMER (v4.11) (Heinz et al., 2010). We used deepTools to draw Pearson's correlation scatter plots for the correlation between replicates of each experiment.

For promoter and enhancer type analysis, H3K27ac ChIP-seq data in wild-type pachytene spermatocytes were downloaded from the published data (GSE107398) (Adams et al., 2018); ChIP-seq data for H3K4me1, H3K4me3, and H3K27me3 in wild-type pachytene spermatocytes were downloaded from the published data (GSE132446) (Chen et al., 2020).

ATAC-seq data analysis. ATAC-seq data were analyzed using a standardized ENCODE ATAC-seq pipeline (v2.2.2, https://github.com/ENCODE-DCC/atac-seq-pipeline). The mouse reference genome (mm10) was used in the pipeline. Trimming, mapping, and duplicate-removing were performed as the ENCODE pipeline suggested using Cutadapt (v2.5) (Kechin et al., 2017), Bowtie2 (v2.3.4.3) (Langmead et al., 2009), and Picard (v2.20.7) (https://broadinstitute.github.io/picard/) respectively. MACS2 (v2.2.4) (Zhang et al., 2008) was used for peak calling.

Statistics and reproducibility. Statistical analyses were performed using R and Prism 9. Data are presented as means ± s.d. unless otherwise indicated. The two-tailed, unpaired, Student's t-test, Mann–Whitney test, or one-way or two-way ANOVA were performed to analyze statistical significance.

Supplementary Materials

This manuscript file includes Figs. S1 to S9 and Tables S1 and S8.

Reference

Adams, S.R., Maezawa, S., Alavattam, K.G., Abe, H., Sakashita, A., Shroder, M., Broering, T.J., Sroga Rios, J., Thomas, M.A., Lin, X.*, et al.* (2018). RNF8 and SCML2 cooperate to regulate ubiquitination and H3K27 acetylation for escape gene activation on the sex chromosomes. PLoS genetics *14*, e1007233.

Aibar, S., Gonzalez-Blas, C.B., Moerman, T., Huynh-Thu, V.A., Imrichova, H., Hulselmans, G., Rambow, F., Marine, J.C., Geurts, P., Aerts, J.*, et al.* (2017). SCENIC: single-cell regulatory network inference and clustering. Nature methods *14*, 1083-1086.

Alavattam, K.G., Abe, H., Sakashita, A., and Namekawa, S.H. (2018). Chromosome Spread Analyses of Meiotic Sex Chromosome Inactivation. Methods in molecular biology (Clifton, NJ) *1861*, 113-129.

Alexander, A.K., Rice, E.J., Lujic, J., Simon, L.E., Tanis, S., Barshad, G., Zhu, L., Lama, J., Cohen, P.E., and Danko, C.G. (2023). A-MYB and BRDT-dependent RNA Polymerase II pause release orchestrates transcriptional regulation in mammalian meiosis. Nature communications *14*.

Baudat, F., Imai, Y., and de Massy, B. (2013). Meiotic recombination in mammals: localization and regulation. Nature reviews Genetics *14*, 794-806.

Belotti, E., Lacoste, N., Simonet, T., Papin, C., Padmanabhan, K., Scionti, I., Gangloff, Y.G., Ramos, L., Dalkara, D., Hamiche, A.*, et al.* (2020). H2A.Z is dispensable for both basal and activated transcription in post-mitotic mouse muscles. Nucleic acids research *48*, 4601-4613.

Bergerat, A., de Massy, B., Gadelle, D., Varoutas, P.C., Nicolas, A., and Forterre, P. (1997). An atypical topoisomerase II from Archaea with implications for meiotic recombination. Nature *386*, 414-417.

551 Boekhout, M., Karasu, M.E., Wang, J., Acquaviva, L., Pratto, F., Brick, K., Eng, D.Y., Xu, J.,
552 Camerini-Otero, R.D., Patel, D.J., *et al.* (2019). REC114 Partner ANKRD31 Controls Number,
553 Timing, and Location of Meiotic DNA Breaks. Molecular cell *74*, 1053-1068 e1058.
554 Bolcun-Filas, E., Bannister, L.A., Barash, A., Schimenti, K.J., Hartford, S.A., Eppig, J.J.,
555 Handel, M.A., Shen, L., and Schimenti, J.C. (2011). A-MYB (MYBL1) transcription factor is a
556 master regulator of male meiosis. Development *138*, 3319-3330.
557 Butler, A., Hoffman, P., Smibert, P., Papalexi, E., and Satija, R. (2018). Integrating single-cell
558 transcriptomic data across different conditions, technologies, and species. Nature
559 biotechnology *36*, 411-420.
560 Cai, Y., Jin, J., Florens, L., Swanson, S.K., Kusch, T., Li, B., Workman, J.L., Washburn, M.P.,
561 Conaway, R.C., and Conaway, J.W. (2005). The mammalian YL1 protein is a shared subunit
562 of the TRRAP/TIP60 histone acetyltransferase and SRCAP complexes. The Journal of
563 biological chemistry *280*, 13665-13670.
564 Cecchini, K., Biasini, A., Yu, T., Saflund, M., Mou, H., Arif, A., Eghbali, A., Colpan, C.,
565 Gainetdinov, I., de Rooij, D.G., *et al.* (2023). The transcription factor TCFL5 responds to
566 A-MYB to elaborate the male meiotic program in mice. Reproduction *165*, 183-196.
567 Chen, Y., Lyu, R.T., Rong, B.W., Zheng, Y.X., Lin, Z., Dai, R.F., Zhang, X., Xie, N.N., Wang,
568 S.Q., Tang, F.C., *et al.* (2020). Refined spatial temporal epigenomic profiling reveals intrinsic
569 connection between PRDM9-mediated H3K4me3 and the fate of double-stranded breaks. Cell
570 research *30*, 256-268.
571 Chen, Y., Zheng, Y., Gao, Y., Lin, Z., Yang, S., Wang, T., Wang, Q., Xie, N., Hua, R., Liu, M.,
572 *et al.* (2018). Single-cell RNA-seq uncovers dynamic processes and critical regulators in

573 mouse spermatogenesis. Cell research *28*, 879-896.

574 Choi, K., Zhao, X., Kelly, K.A., Venn, O., Higgins, J.D., Yelina, N.E., Hardcastle, T.J.,

575 Ziolkowski, P.A., Copenhaver, G.P., Franklin, F.C.*, et al.* (2013). Arabidopsis meiotic

576 crossover hot spots overlap with H2A.Z nucleosomes at gene promoters. Nature genetics *45*,

577 1327-1336.

578 Colino-Sanguino, Y., Clark, S.J., and Valdes-Mora, F. (2022). The H2A.Z-nuclesome code in

579 mammals: emerging functions. Trends in genetics : TIG *38*, 273-289.

580 Cuadrado, A., Corrado, N., Perdiguero, E., Lafarga, V., Munoz-Canoves, P., and Nebreda,

581 A.R. (2010). Essential role of p18Hamlet/SRCAP-mediated histone H2A.Z chromatin

582 incorporation in muscle differentiation. The EMBO journal *29*, 2014-2025.

583 Cuadrado, A., Lafarga, V., Cheung, P.C., Dolado, I., Llanos, S., Cohen, P., and Nebreda, A.R.

584 (2007). A new p38 MAP kinase-regulated transcriptional coactivator that stimulates

585 p53-dependent apoptosis. The EMBO journal *26*, 2115-2126.

586 Dong, S., Han, J., Chen, H., Liu, T., Huen, M.S., Yang, Y., Guo, C., and Huang, J. (2014). The

587 Human SRCAP Chromatin Remodeling Complex Promotes DNA-End Resection. Current

588 biology : CB *24*, 2097-2110.

589 Ernst, C., Eling, N., Martinez-Jimenez, C.P., Marioni, J.C., and Odom, D.T. (2019). Staged

590 developmental mapping and X chromosome transcriptional dynamics during mouse

591 spermatogenesis. Nature communications *10*, 1251.

592 Ernst, J., and Kellis, M. (2012). ChromHMM: automating chromatin-state discovery and

593 characterization. Nature methods *9*, 215-216.

594 Feng, Y., Zhang, Y., Lin, Z., Ye, X., Lin, X., Lv, L., Lin, Y., Sun, S., Qi, Y., and Lin, X. (2022).

595 Chromatin remodeler Dmp18 regulates apoptosis by controlling H2Av incorporation in
596 Drosophila imaginal disc development. PLoS genetics *18*, e1010395.
597 Gaucher, J., Boussouar, F., Montellier, E., Curtet, S., Buchou, T., Bertrand, S., Hery, P.,
598 Jounier, S., Depaux, A., Vitte, A.L.*, et al.* (2012). Bromodomain-dependent stage-specific male
599 genome programming by Brdt. The EMBO journal *31*, 3809-3820.
600 Gray, S., and Cohen, P.E. (2016). Control of Meiotic Crossovers: From Double-Strand Break
601 Formation to Designation. Annu Rev Genet *50*, 175-210.
602 Green, C.D., Ma, Q., Manske, G.L., Shami, A.N., Zheng, X., Marini, S., Moritz, L., Sultan, C.,
603 Gurczynski, S.J., Moore, B.B.*, et al.* (2018). A Comprehensive Roadmap of Murine
604 Spermatogenesis Defined by Single-Cell RNA-Seq. Developmental cell *46*, 651-667 e610.
605 Gu, Z., and Hubschmann, D. (2023). rGREAT: an R/bioconductor package for functional
606 enrichment on genomic regions. Bioinformatics *39*.
607 Handel, M.A., and Schimenti, J.C. (2010). Genetics of mammalian meiosis: regulation,
608 dynamics and impact on fertility. Nature reviews Genetics *11*, 124-136.
609 Hassold, T., and Hunt, P. (2001). To err (meiotically) is human: the genesis of human
610 aneuploidy. Nature reviews Genetics *2*, 280-291.
611 Heinz, S., Benner, C., Spann, N., Bertolino, E., Lin, Y.C., Laslo, P., Cheng, J.X., Murre, C.,
612 Singh, H., and Glass, C.K. (2010). Simple combinations of lineage-determining transcription
613 factors prime cis-regulatory elements required for macrophage and B cell identities. Molecular
614 cell *38*, 576-589.
615 Hirota, T., Blakeley, P., Sangrithi, M.N., Mahadevaiah, S.K., Encheva, V., Snijders, A.P.,
616 Ellnati, E., Ojarikre, O.A., de Rooij, D.G., Niakan, K.K.*, et al.* (2018). SETDB1 Links the Meiotic

617 DNA Damage Response to Sex Chromosome Silencing in Mice. Developmental cell *47*,
618 645-+.
619 Huang, Y., and Roig, I. (2023). Genetic control of meiosis surveillance mechanisms in
620 mammals. Front Cell Dev Biol *11*, 1127440.
621 Hunter, N. (2015). Meiotic Recombination: The Essence of Heredity. Cold Spring Harbor
622 perspectives in biology *7*.
623 Kechin, A., Boyarskikh, U., Kel, A., and Filipenko, M. (2017). cutPrimers: A New Tool for
624 Accurate Cutting of Primers from Reads of Targeted Next Generation Sequencing. J Comput
625 Biol *24*, 1138-1143.
626 Keeney, S., Giroux, C.N., and Kleckner, N. (1997). Meiosis-specific DNA double-strand breaks
627 are catalyzed by Spo11, a member of a widely conserved protein family. Cell *88*, 375-384.
628 Kim, D., Langmead, B., and Salzberg, S.L. (2015). HISAT: a fast spliced aligner with low
629 memory requirements. Nature methods *12*, 357-360.
630 Kim, D., Paggi, J.M., Park, C., Bennett, C., and Salzberg, S.L. (2019). Graph-based genome
631 alignment and genotyping with HISAT2 and HISAT-genotype. Nature biotechnology *37*,
632 907-915.
633 Kota, S.K., and Feil, R. (2010). Epigenetic transitions in germ cell development and meiosis.
634 Developmental cell *19*, 675-686.
635 Langmead, B., Trapnell, C., Pop, M., and Salzberg, S.L. (2009). Ultrafast and memory-efficient
636 alignment of short DNA sequences to the human genome. Genome biology *10*, R25.
637 Lascarez-Lagunas, L., Martinez-Garcia, M., and Colaiacovo, M. (2020). SnapShot: Meiosis -
638 Prophase I. Cell *181*, 1442-1442 e1441.

639 Latendresse, J.R., Warbrittion, A.R., Jonassen, H., and Creasy, D.M. (2002). Fixation of testes
640 and eyes using a modified Davidson's fluid: comparison with Bouin's fluid and conventional
641 Davidson's fluid. Toxicol Pathol *30*, 524-533.
642 Law, N.C., Oatley, M.J., and Oatley, J.M. (2019). Developmental kinetics and transcriptome
643 dynamics of stem cell specification in the spermatogenic lineage. Nature communications *10*,
644 2787.
645 Li, H., and Durbin, R. (2009). Fast and accurate short read alignment with Burrows-Wheeler
646 transform. Bioinformatics *25*, 1754-1760.
647 Li, H., Handsaker, B., Wysoker, A., Fennell, T., Ruan, J., Homer, N., Marth, G., Abecasis, G.,
648 Durbin, R., and Genome Project Data Processing, S. (2009). The Sequence Alignment/Map
649 format and SAMtools. Bioinformatics *25*, 2078-2079.
650 Li, X.Z., Roy, C.K., Dong, X., Bolcun-Filas, E., Wang, J., Han, B.W., Xu, J., Moore, M.J.,
651 Schimenti, J.C., Weng, Z.*, et al.* (2013). An ancient transcription factor initiates the burst of
652 piRNA production during early meiosis in mouse testes. Molecular cell *50*, 67-81.
653 Lin, Z., Hsu, P.J., Xing, X., Fang, J., Lu, Z., Zou, Q., Zhang, K.J., Zhang, X., Zhou, Y., Zhang,
654 T.*, et al.* (2017). Mettl3-/Mettl14-mediated mRNA N6-methyladenosine modulates murine
655 spermatogenesis. Cell research.
656 Long, J., Huang, C., Chen, Y., Zhang, Y., Shi, S., Wu, L., Liu, Y., Liu, C., Wu, J., and Lei, M.
657 (2017). Telomeric TERB1-TRF1 interaction is crucial for male meiosis. Nat Struct Mol Biol *24*,
658 1073-1080.
659 Love, M.I., Huber, W., and Anders, S. (2014). Moderated estimation of fold change and
660 dispersion for RNA-seq data with DESeq2. Genome biology *15*, 550.

661 Lu, J., An, J., Wang, J., Cao, X., Cao, Y., Huang, C., Jiao, S., Yan, D., Lin, X., and Zhou, X.
662 (2022). Znhit1 Regulates p21Cip1 to Control Mouse Lens Differentiation. Investigative
663 ophthalmology & visual science *63*, 18.
664 Maezawa, S., Sakashita, A., Yukawa, M., Chen, X., Takahashi, K., Alavattam, K.G., Nakata, I.,
665 Weirauch, M.T., Barski, A., and Namekawa, S.H. (2020). Super-enhancer switching drives a
666 burst in gene expression at the mitosis-to-meiosis transition. Nat Struct Mol Biol *27*, 978-988.
667 Manterola, M., Brown, T.M., Oh, M.Y., Garyn, C., Gonzalez, B.J., and Wolgemuth, D.J. (2018).
668 BRDT is an essential epigenetic regulator for proper chromatin organization, silencing of sex
669 chromosomes and crossover formation in male meiosis. PLoS genetics *14*, e1007209.
670 Marcet-Ortega, M., Pacheco, S., Martinez-Marchal, A., Castillo, H., Flores, E., Jasin, M.,
671 Keeney, S., and Roig, I. (2017). p53 and TAp63 participate in the recombination-dependent
672 pachytene arrest in mouse spermatocytes. PLoS genetics *13*, e1006845.
673 Mytlis, A., Kumar, V., Qiu, T., Deis, R., Hart, N., Levy, K., Masek, M., Shawahny, A., Ahmad, A.,
674 Eitan, H.*, et al.* (2022). Control of meiotic chromosomal bouquet and germ cell morphogenesis
675 by the zygotene cilium. Science, eabh3104.
676 Ozata, D.M., Yu, T., Mou, H., Gainetdinov, I., Colpan, C., Cecchini, K., Kaymaz, Y., Wu, P.H.,
677 Fan, K., Kucukural, A.*, et al.* (2020). Evolutionarily conserved pachytene piRNA loci are highly
678 divergent among modern humans. Nat Ecol Evol *4*, 156-168.
679 Papanikos, F., Clement, J.A.J., Testa, E., Ravindranathan, R., Grey, C., Dereli, I., Bondarieva,
680 A., Valerio-Cabrera, S., Stanzione, M., Schleiffer, A.*, et al.* (2019). Mouse ANKRD31
681 Regulates Spatiotemporal Patterning of Meiotic Recombination Initiation and Ensures
682 Recombination between X and Y Sex Chromosomes. Molecular cell *74*, 1069-1085 e1011.

683 Pertea, M., Kim, D., Pertea, G.M., Leek, J.T., and Salzberg, S.L. (2016). Transcript-level
684 expression analysis of RNA-seq experiments with HISAT, StringTie and Ballgown. Nature
685 protocols *11*, 1650-1667.
686 Pertea, M., Pertea, G.M., Antonescu, C.M., Chang, T.C., Mendell, J.T., and Salzberg, S.L.
687 (2015). StringTie enables improved reconstruction of a transcriptome from RNA-seq reads.
688 Nature biotechnology *33*, 290-295.
689 Qiao, H., Prasada Rao, H.B., Yang, Y., Fong, J.H., Cloutier, J.M., Deacon, D.C., Nagel, K.E.,
690 Swartz, R.K., Strong, E., Holloway, J.K.*, et al.* (2014). Antagonistic roles of ubiquitin ligase
691 HEI10 and SUMO ligase RNF212 regulate meiotic recombination. Nature genetics *46*,
692 194-199.
693 Rabbani, M., Zheng, X., Manske, G.L., Vargo, A., Shami, A.N., Li, J.Z., and Hammoud, S.S.
694 (2022). Decoding the Spermatogenesis Program: New Insights from Transcriptomic Analyses.
695 Annu Rev Genet *56*, 339-368.
696 Ramirez, F., Dundar, F., Diehl, S., Gruning, B.A., and Manke, T. (2014). deepTools: a flexible
697 platform for exploring deep-sequencing data. Nucleic acids research *42*, W187-191.
698 Rao, H.B., Qiao, H., Bhatt, S.K., Bailey, L.R., Tran, H.D., Bourne, S.L., Qiu, W., Deshpande, A.,
699 Sharma, A.N., Beebout, C.J.*, et al.* (2017). A SUMO-ubiquitin relay recruits proteasomes to
700 chromosome axes to regulate meiotic recombination. Science *355*, 403-407.
701 Reynolds, A., Qiao, H.Y., Yang, Y., Chen, J.K., Jackson, N., Biswas, K., Holloway, J.K.,
702 Baudat, F., de Massy, B., Wang, J.*, et al.* (2013). RNF212 is a dosage-sensitive regulator of
703 crossing-over during mammalian meiosis. Nature genetics *45*, 269-278.
704 Roeder, G.S., and Bailis, J.M. (2000). The pachytene checkpoint. Trends in genetics : TIG *16*,

705 395-403.

706 Royo, H., Prosser, H., Ruzankina, Y., Mahadevaiah, S.K., Cloutier, J.M., Baumann, M.,

707 Fukuda, T., Hoog, C., Toth, A., de Rooij, D.G.*, et al.* (2013). ATR acts stage specifically to

708 regulate multiple aspects of mammalian meiotic silencing. Genes & development *27*,

709 1484-1494.

710 San Filippo, J., Sung, P., and Klein, H. (2008). Mechanism of eukaryotic homologous

711 recombination. Annual review of biochemistry *77*, 229-257.

712 Shibuya, H., Ishiguro, K., and Watanabe, Y. (2014). The TRF1-binding protein TERB1

713 promotes chromosome movement and telomere rigidity in meiosis. Nature cell biology *16*,

714 145-156.

715 Spruce, C., Dlamini, S., Ananda, G., Bronkema, N., Tian, H., Paigen, K., Carter, G.W., and

716 Baker, C.L. (2020). HELLS and PRDM9 form a pioneer complex to open chromatin at meiotic

717 recombination hot spots. Genes & development *34*, 398-412.

718 Subramanian, A., Tamayo, P., Mootha, V.K., Mukherjee, S., Ebert, B.L., Gillette, M.A.,

719 Paulovich, A., Pomeroy, S.L., Golub, T.R., Lander, E.S.*, et al.* (2005). Gene set enrichment

720 analysis: a knowledge-based approach for interpreting genome-wide expression profiles.

721 Proceedings of the National Academy of Sciences of the United States of America *102*,

722 15545-15550.

723 Subramanian, V.V., and Hochwagen, A. (2014). The meiotic checkpoint network: step-by-step

724 through meiotic prophase. Cold Spring Harbor perspectives in biology *6*, a016675.

725 Sun, S., Jiang, N., Jiang, Y., He, Q., He, H., Wang, X., Yang, L., Li, R., Liu, F., Lin, X.*, et al.*

726 (2020). Chromatin remodeler Znhit1 preserves hematopoietic stem cell quiescence by

727 determining the accessibility of distal enhancers. Leukemia *34*, 3348-3358.

728 Sun, S., Jiang, Y., Zhang, Q., Pan, H., Li, X., Yang, L., Huang, M., Wei, W., Wang, X., Qiu, M.*,*

729 *et al.* (2022). Znhit1 controls meiotic initiation in male germ cells by coordinating with Stra8 to

730 activate meiotic gene expression. Developmental cell *57*, 901-913 e904.

731 Symington, L.S. (2014). End resection at double-strand breaks: mechanism and regulation.

732 Cold Spring Harbor perspectives in biology *6*.

733 Turner, J.M. (2015). Meiotic Silencing in Mammals. Annu Rev Genet *49*, 395-412.

734 Turner, J.M., Mahadevaiah, S.K., Fernandez-Capetillo, O., Nussenzweig, A., Xu, X., Deng,

735 C.X., and Burgoyne, P.S. (2005). Silencing of unsynapsed meiotic chromosomes in the mouse.

736 Nature genetics *37*, 41-47.

737 Wang, L., Xu, Z., Khawar, M.B., Liu, C., and Li, W. (2017). The histone codes for meiosis.

738 Reproduction *154*, R65-R79.

739 Wang, Y., Chen, Y., Chen, J., Wang, L., Nie, L., Long, J., Chang, H., Wu, J., Huang, C., and

740 Lei, M. (2019). The meiotic TERB1-TERB2-MAJIN complex tethers telomeres to the nuclear

741 envelope. Nature communications *10*, 564.

742 Wang, Y., and Copenhaver, G.P. (2018). Meiotic Recombination: Mixing It Up in Plants. Annu

743 Rev Plant Biol *69*, 577-609.

744 Wei, W., Tang, X., Jiang, N., Ni, C., He, H., Sun, S., Yu, M., Yu, C., Qiu, M., Yan, D.*, et al.*

745 (2022). Chromatin remodeler Znhit1 controls bone morphogenetic protein signaling in

746 embryonic lung tissue branching. The Journal of biological chemistry *298*, 102490.

747 Wu, T., Hu, E., Xu, S., Chen, M., Guo, P., Dai, Z., Feng, T., Zhou, L., Tang, W., Zhan, L.*, et al.*

748 (2021). clusterProfiler 4.0: A universal enrichment tool for interpreting omics data. Innovation

749 (Camb) *2*, 100141.

750 Wu, T., Lyu, R., You, Q., and He, C. (2020). Kethoxal-assisted single-stranded DNA

751 sequencing captures global transcription dynamics and enhancer activity in situ. Nature

752 methods *17*, 515-523.

753 Xu, M., Yao, J., Shi, Y., Yi, H., Zhao, W., Lin, X., and Yang, Z. (2021). The SRCAP chromatin

754 remodeling complex promotes oxidative metabolism during prenatal heart development.

755 Development *148*.

756 Xu, Y., Ayrapetov, M.K., Xu, C., Gursoy-Yuzugullu, O., Hu, Y., and Price, B.D. (2012). Histone

757 H2A.Z controls a critical chromatin remodeling step required for DNA double-strand break

758 repair. Molecular cell *48*, 723-733.

759 Yamada, S., Kugou, K., Ding, D.Q., Fujita, Y., Hiraoka, Y., Murakami, H., Ohta, K., and

760 Yamada, T. (2018). The histone variant H2A.Z promotes initiation of meiotic recombination in

761 fission yeast. Nucleic acids research *46*, 609-620.

762 Yoshida, S., Sukeno, M., Nakagawa, T., Ohbo, K., Nagamatsu, G., Suda, T., and Nabeshima,

763 Y. (2006). The first round of mouse spermatogenesis is a distinctive program that lacks the

764 self-renewing spermatogonia stage. Development *133*, 1495-1505.

765 Yoshida, S., Takakura, A., Ohbo, K., Abe, K., Wakabayashi, J., Yamamoto, M., Suda, T., and

766 Nabeshima, Y. (2004). Neurogenin3 delineates the earliest stages of spermatogenesis in the

767 mouse testis. Developmental biology *269*, 447-458.

768 Yu, T., Fan, K., Ozata, D.M., Zhang, G., Fu, Y., Theurkauf, W.E., Zamore, P.D., and Weng, Z.

769 (2021). Long first exons and epigenetic marks distinguish conserved pachytene piRNA

770 clusters from other mammalian genes. Nature communications *12*, 73.

771 Zhang, Q., Ji, S.Y., Busayavalasa, K., and Yu, C. (2019). SPO16 binds SHOC1 to promote
772 homologous recombination and crossing-over in meiotic prophase I. Sci Adv *5*, eaau9780.
773 Zhang, Y., Liu, T., Meyer, C.A., Eeckhoute, J., Johnson, D.S., Bernstein, B.E., Nusbaum, C.,
774 Myers, R.M., Brown, M., Li, W.*, et al.* (2008). Model-based analysis of ChIP-Seq (MACS).
775 Genome biology *9*, R137.
776 Zhao, B., Chen, Y., Jiang, N., Yang, L., Sun, S., Zhang, Y., Wen, Z., Ray, L., Liu, H., Hou, G.*,*
777 *et al.* (2019). Znhit1 controls intestinal stem cell maintenance by regulating H2A.Z
778 incorporation. Nature communications *10*, 1071.
779 Zheng, H., and Xie, W. (2019). The role of 3D genome organization in development and cell
780 differentiation. Nature reviews Molecular cell biology.
781 Zickler, D., and Kleckner, N. (2023). Meiosis: Dances Between Homologs. Annu Rev Genet.
782
783

Acknowledgments: We thank Chuan He for N3-kethoxal and Christopher L. Baker for meiotic chromatin state data. **Funding:** This work was supported by grants from the National Key Research and Development Program of China (2022YFA0806200, 2018YFC1003500, 2018YFA0800100, 2021YFC2501800), the National Natural Science Foundation of China (32192403, 81971443, 32300702), the Science and Technology Major Project of Inner Mongolia Autonomous Region of China to the State Key Laboratory of Reproductive Regulation and Breeding of Grassland Livestock (2020ZD0008), and the China Postdoctoral Science Foundation (2022M720797).

Author Contributions: S.S. and X.L. conceived and designed the study; S.S. performed most of the experiments with the help of Y.J., Q.Z., H.P., F.H., X.Z., Y.G., X.Y., K.G., W.W., H.L., Z.S., Y.S., X.T., M.Y., and R.L.; Y.J. and N.J. performed the bioinformatics analysis; X.L. supervised the work and acquired the funding support; and S.S. and X.L. wrote the manuscript, with contributions from all authors. **Competing interests:** The authors declare that they have no competing interests. **Data and materials availability:** The NGS data generated in this study were deposited to the NCBI SRA database under accession numbers SRP467214 (RNA-seq and ChIP-seq data) and SRP467448 (ATAC-seq and KAS-seq data).

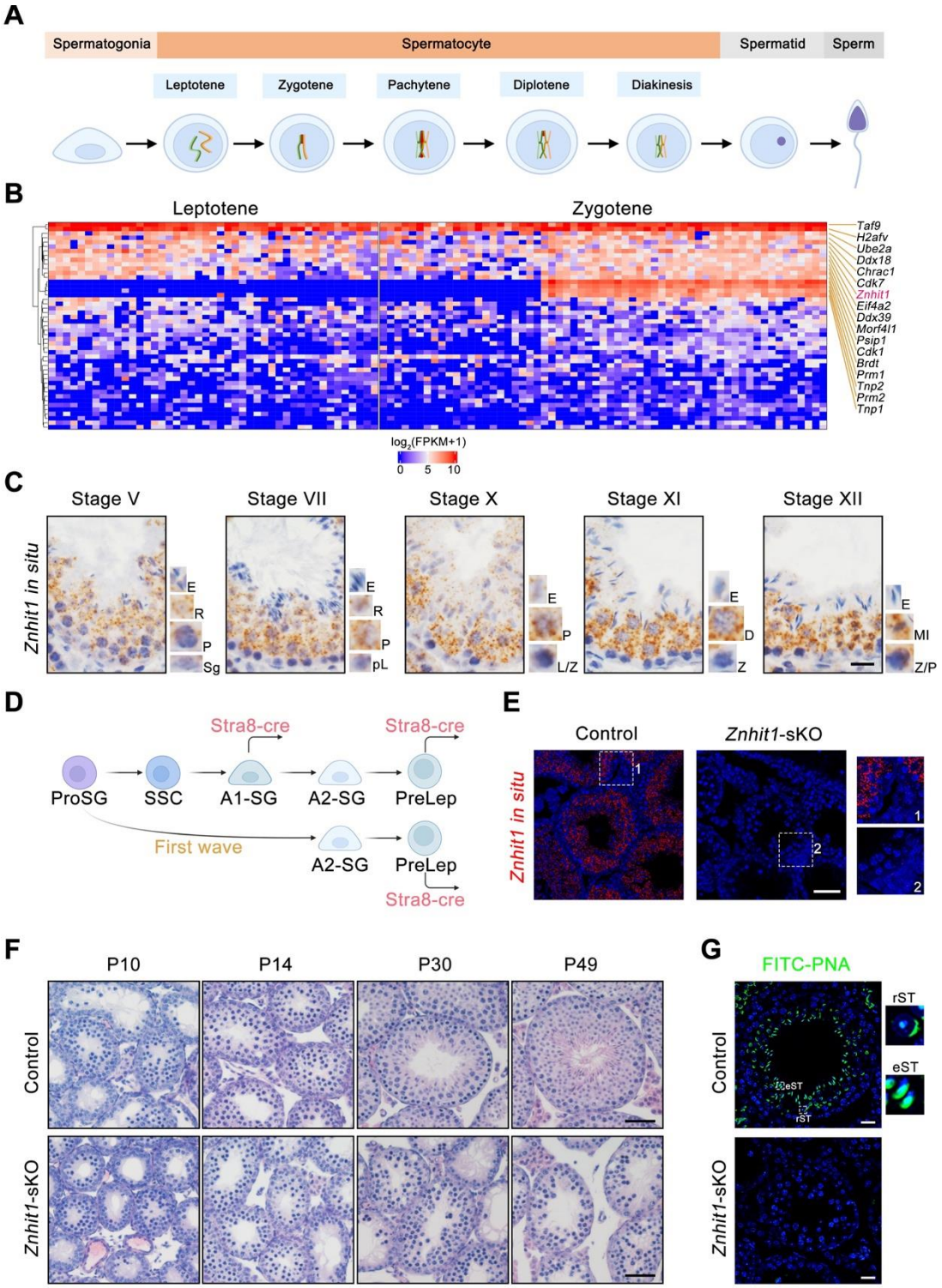

Figure 1 | Znhit1 deletion in spermatocytes disrupts spermatogenesis. (**A**) Schematic representation of the male germline development in mice. (**B**) Heatmap showing the clustering of 47 epigenetic factors based on the transcription levels in leptotene and zygotene spermatocytes. (**C**) *Znhit1* in situ hybridization in postnatal day 60 (P60) testis sections. Scale bar, 20 μm. Sg, spermatogonia; pL, preleptotene; L, leptotene; Z, zygotene;

P, pachytene; D, diplotene, MI, metaphase; R, round spermatids; E, elongating spermatids. (**D**) Schematic diagram showing the onset of Stra8-cre expression in the male germline development. (**E**) *Znhit1* in situ hybridization in P42 testis sections. Scale bar, 50 μm. (**F**) Histological testicular sections in control or *Znhit1*-sKO testis sections at the indicated times. Scale bar, 50 μm. (**G**) Immunostaining of PNA in testis sections from control or *Znhit1*-sKO mice at the indicated times. rST, round spermatids; eST, elongating spermatids. Scale bar, 20 μm. All images are representative of n = 3 mice per genotype.

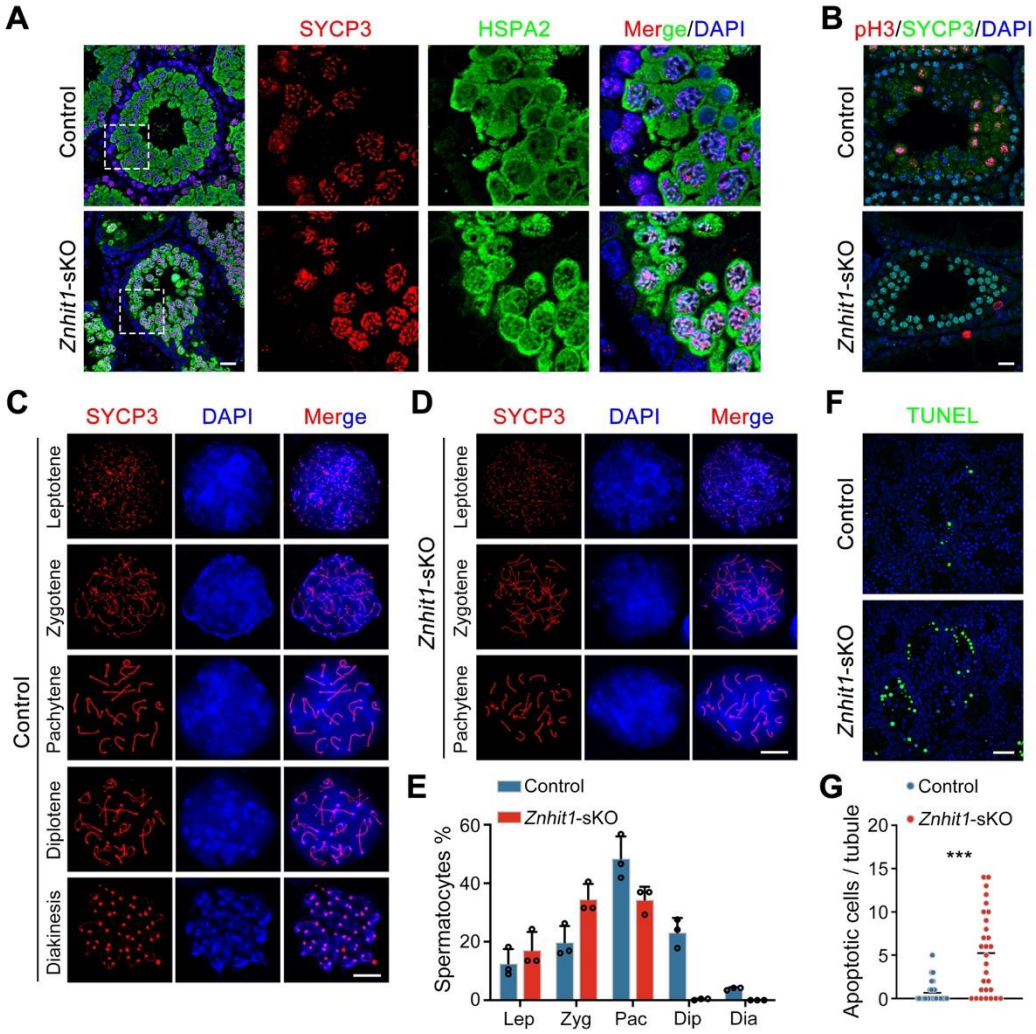

Figure 2 | Znhit1 deletion leads to meiotic pachytene arrest. (**A**) Immunostaining of SYCP3 and HSPA2 in testis sections of P35 control or *Znhit1*-sKO mice. Scale bar, 20 µm. (**B**) Immunostaining of SYCP3 and pH3 in testis sections of P35 control or *Znhit1*-sKO mice. Scale bar, 20 µm. (**C**-**E**) Immunostaining of SYCP3 in spermatocyte chromosome spreads of control (**C**) or *Znhit1*-sKO mice (**D**). Quantitative data are shown in (**E**). Scale bar, 10 µm. (**F** and **G**) TUNEL staining in testis sections from P14 control or *Znhit1*-CKO mice. Quantitative data are shown in (**G**). Scale bar, 40 µm. All images are representative of n = 3 mice per genotype. Data are presented as the mean ± s.d. *** $p < 0.001$.

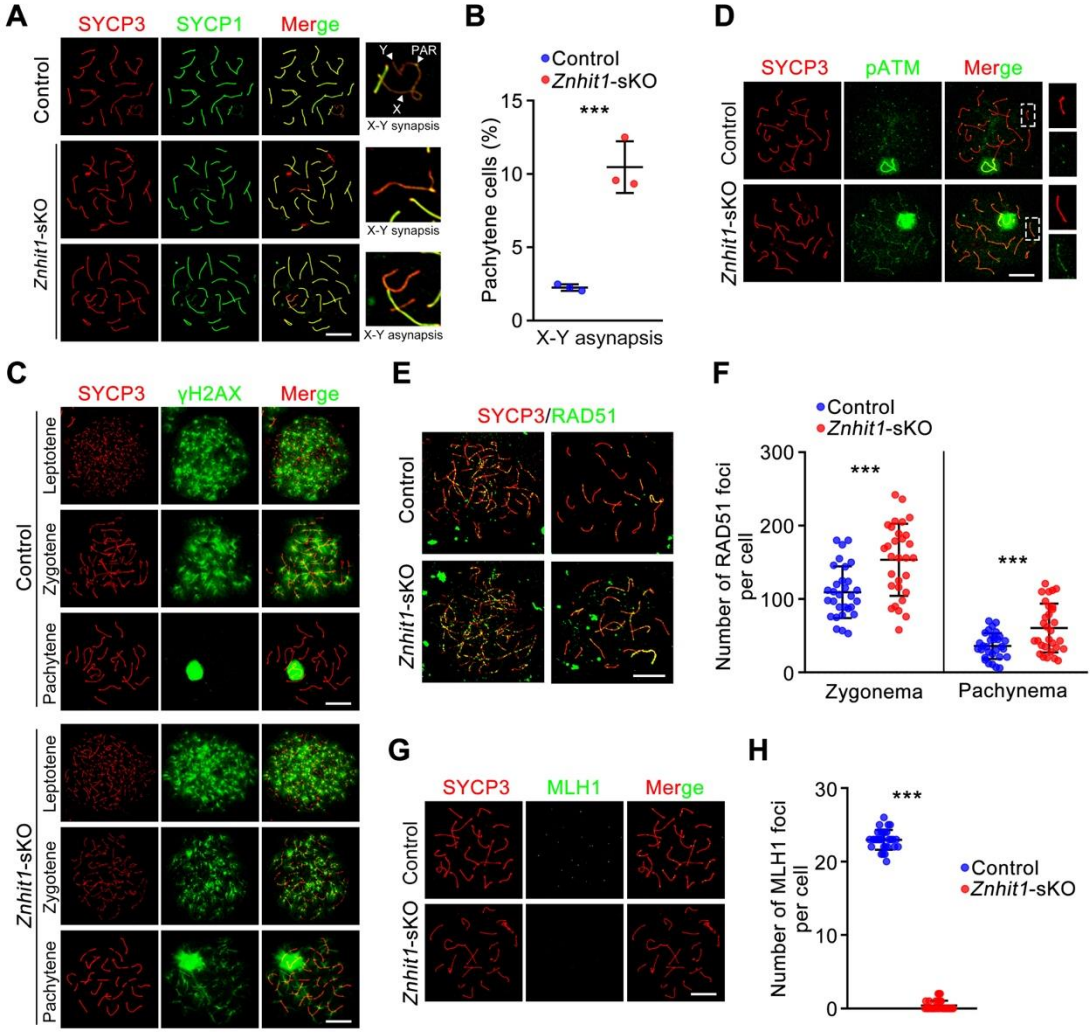

Figure 3 | Znhit1 controls meiotic recombination. (**A** and **B**) Immunostaining of SYCP3 and SYCP1 in spermatocyte chromosome spreads of control or *Znhit1*-sKO mice. X, X chromosome; Y, Y chromosome; PAR, pseudoautosomal region. Quantitative data are shown in (**B**). Scale bar, 10 μm. (**C**) Immunostaining of SYCP3 and γH2AX in spermatocyte chromosome spreads of control or *Znhit1*-sKO mice. Scale bar, 10 μm. (**D**) Immunostaining of SYCP3 and pATM in spermatocyte chromosome spreads of control or *Znhit1*-sKO mice. Scale bar, 10 μm. (**E** and **F**) Immunostaining of SYCP3 and RAD51 in spermatocyte chromosome spreads of control or *Znhit1*-sKO mice. Quantitative data are shown in (**F**). Scale bar, 10 μm. (**G** and **H**) Immunostaining of SYCP3 and MLH1 in spermatocyte chromosome spreads of control or *Znhit1*-sKO mice. Quantitative data are shown in (**H**). Scale bar, 10 μm. All images are representative of n = 3 mice per genotype. Data are presented as the mean ± s.d. *** $p < 0.001$.

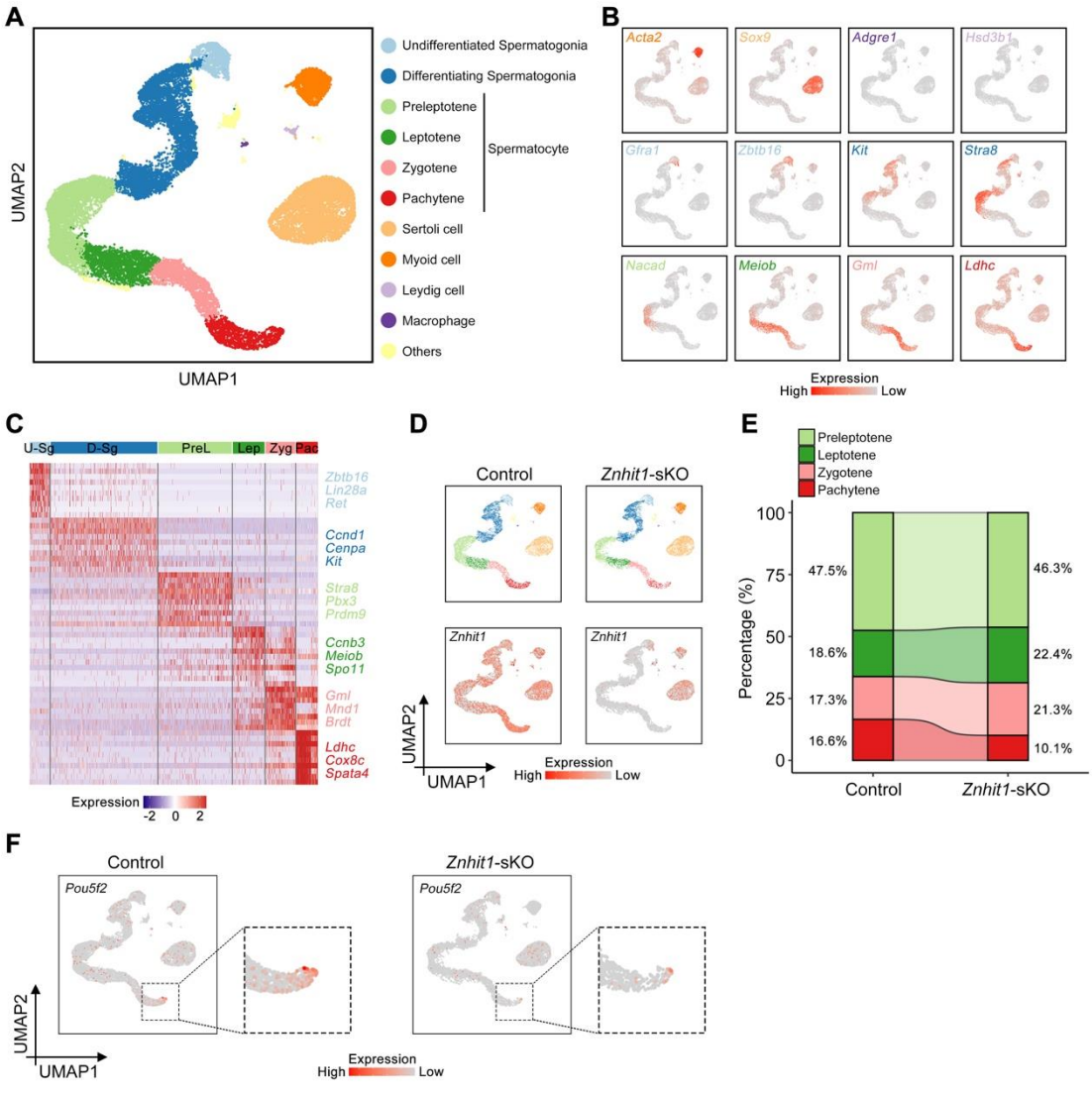

Figure 4 | Spermatocyte transcriptome analysis using scRNA-seq. (**A**) UMAP plot showing the annotated germ cells captured from both control and *Znhit1*-sKO testicular cells. (**B**) Expression of selected markers identifying major somatic cell types and germ cell types on the UMAP plot. UMAP plot showing the expression patterns of *Znhit1* in control or *Znhit1*-sKO testicular cells. (**C**) Heatmap showing the top marker genes of each cell cluster from scRNA-seq data. U-Sg, undifferentiated spermatogonia; D-Sg, differentiating spermatogonia; PreL, preleptotene; Lep, leptotene; Zyg, zygotene; Pac, pachytene. (**D**) Top: UMAP plot showing the annotated germ cells captured from control or *Znhit1*-sKO testicular cells. Down: UMAP plot showing the expression patterns of *Znhit1* in control or *Znhit1*-sKO testicular cells. (**E**) Bar plot showing the percentage of major spermatocyte types for control or *Znhit1*-sKO testicular cells. (**F**) UMAP plot

showing the expression patterns of *Pou5f2* in control or *Znhit1*-sKO germ cells.

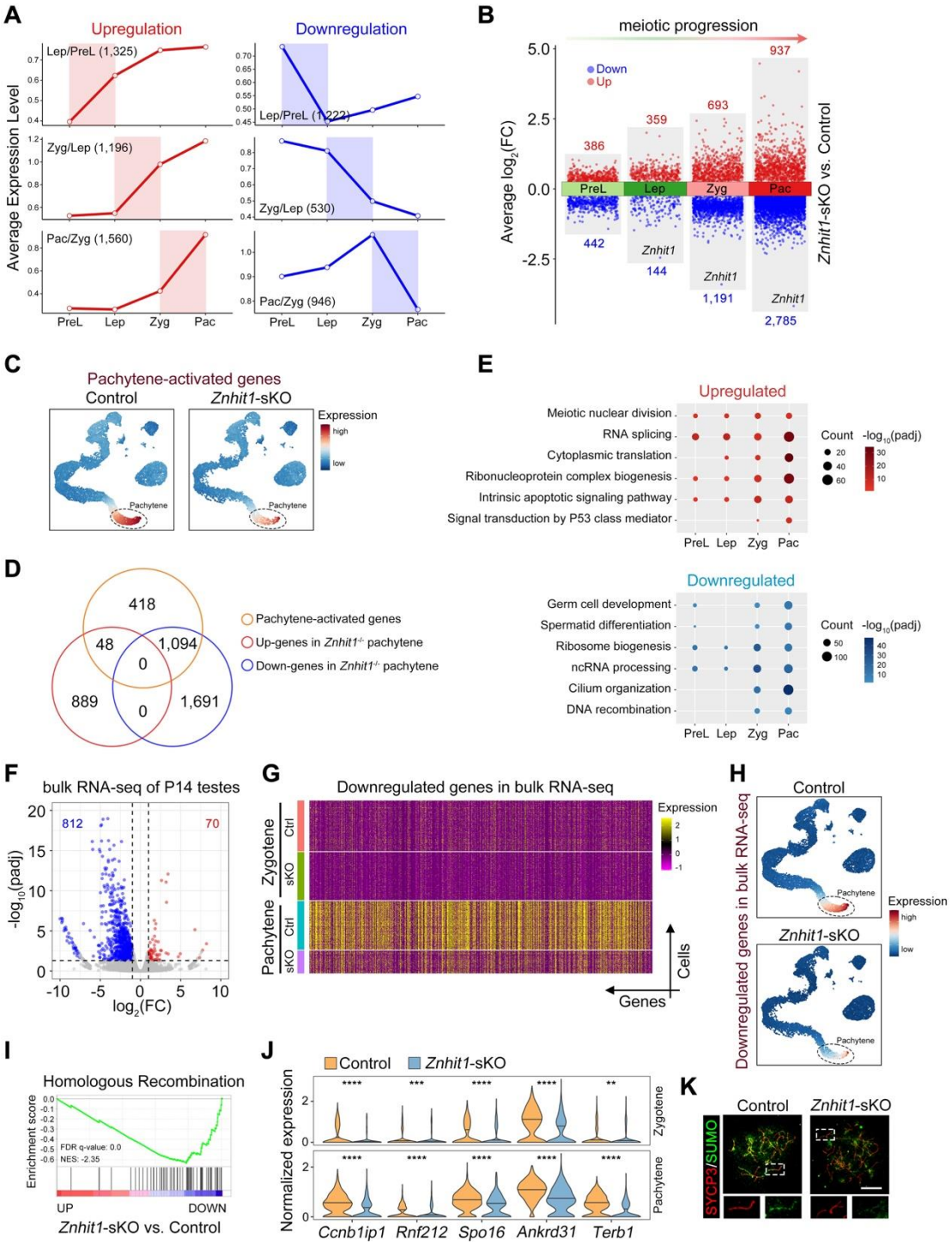

Figure 5 | Znhit1 deletion impairs meiotic transcriptional activation. (**A**) Line graph showing DEGs (upregulation or downregulation) in two consecutive spermatocyte stages. PreL, preleptotene; Lep, leptotene; Zyg, zygotene; Pac, pachytene. (**B**) Volcano plot showing the distribution of upregulated and downregulated DEGs for each cell type in spermatocytes between control or *Znhit1*-sKO testicular cells. (**C**) Cluster annotation on the basis of the expression of pachytene-activated genes in control or *Znhit1*-sKO

testicular cells. (**D**) Venn plots showing the number of shared genes between pachytene-activated genes and DEGs in *Znhit1*-sKO pachytene spermatocytes. (**E**) Representative shared Gene Ontology (GO) terms of upregulated (upper) and downregulated (lower) DEGs at consecutive spermatocyte stages. (**F**) Volcano plot showing differentially expressed genes (DEGs) in bulk RNA-seq following Znhit1 deletion (n = 2). (**G**) Heatmap depicting the expression of the indicated genes at the zygotene and pachytene stages in the scRNA-seq data. (**H**) Cluster annotation on the basis of the expression of downregulated genes in bulk RNA-seq between control and *Znhit1*-sKO testicular cells. (**I**) GSEA of RNA-seq data for the control and *Znhit1*-sKO testicular cells. Selected gene sets encoded products related to homologous recombination. (**J**) Violin plots showing downregulated DEGs of Znhit1-deficient zygotene cells and pachytene cells related to homologous recombination. (**K**) Immunostaining of SYCP3 and SUMO2/3 in spermatocyte chromosome spreads of control or *Znhit1*-sKO mice. Scale bar, 10 μm. cluster genes. ** $p < 0.01$, *** $p < 0.001$, **** $p < 0.0001$.

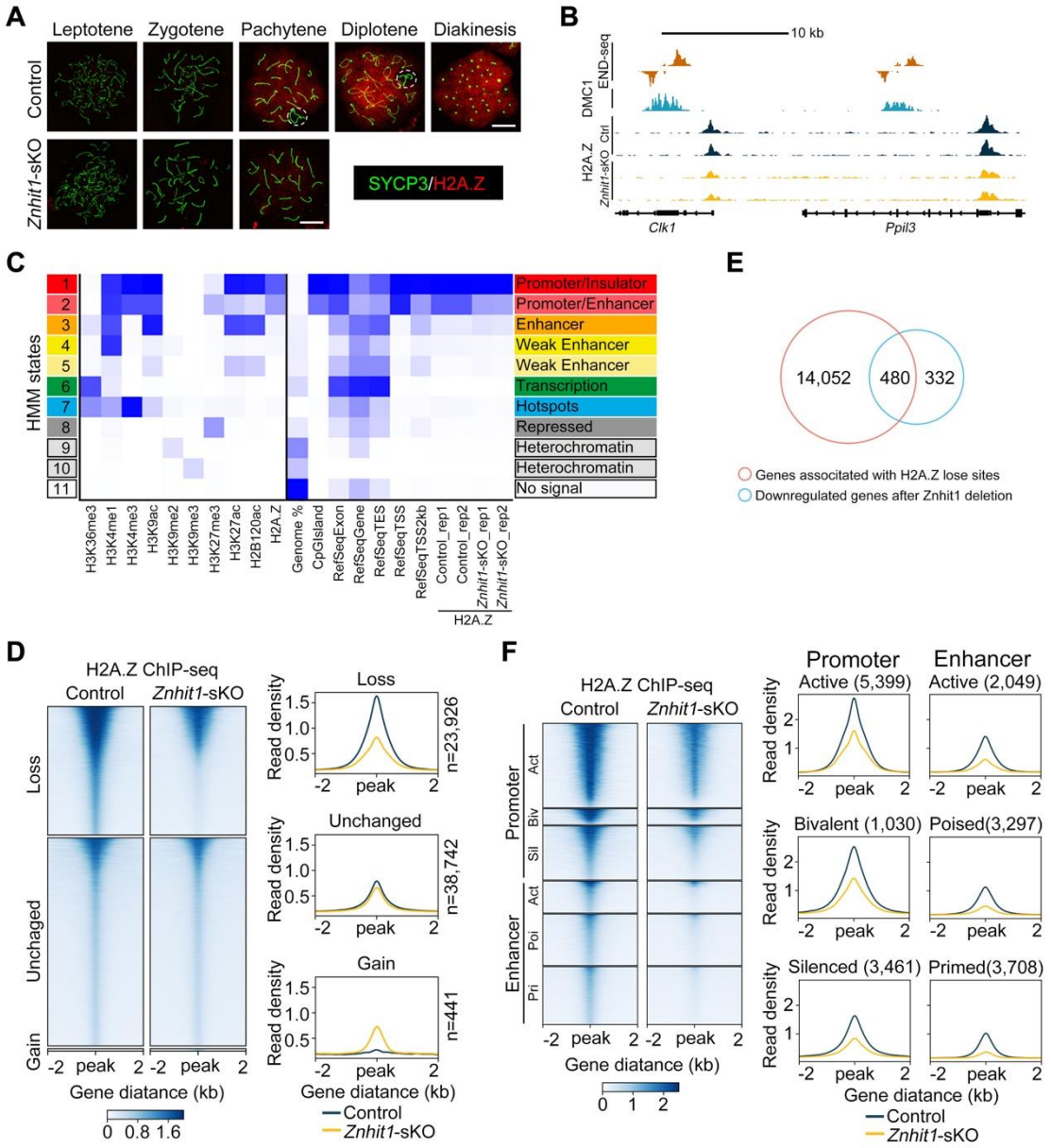

Figure 6 | Znhit1 regulates H2A.Z binding on promoter and enhancer regions. (**A**) Immunostaining of SYCP3 and H2A.Z in spermatocyte chromosome spreads of control or *Znhit1*-sKO mice. The dashed circle indicates X-Y chromosomes. Scale bar, 10 μm. (**B**) Representative tracks of END-seq, DMC1-SSDS, and H2A.Z ChIP-seq in wild-type, control, or *Znhit1*-sKO testicular cells. (**C**) Heatmaps of chromatin states produced by ChromHMM and showing different enrichment for H2A.Z in control or *Znhit1*-sKO testicular cells. (**D**) Heatmaps and mean plots of H2A.Z ChIP-seq signal in control or *Znhit1*-sKO testicular cells (n = 2). (**E**) Venn diagram showing the overlap between decreased H2A.Z-bound genes and downregulated genes in *Znhit1*-sKO testicular cells.

(**F**) Heatmaps and mean plots of downregulated H2A.Z ChIP-seq signals surrounding different types of promoters and enhancers.

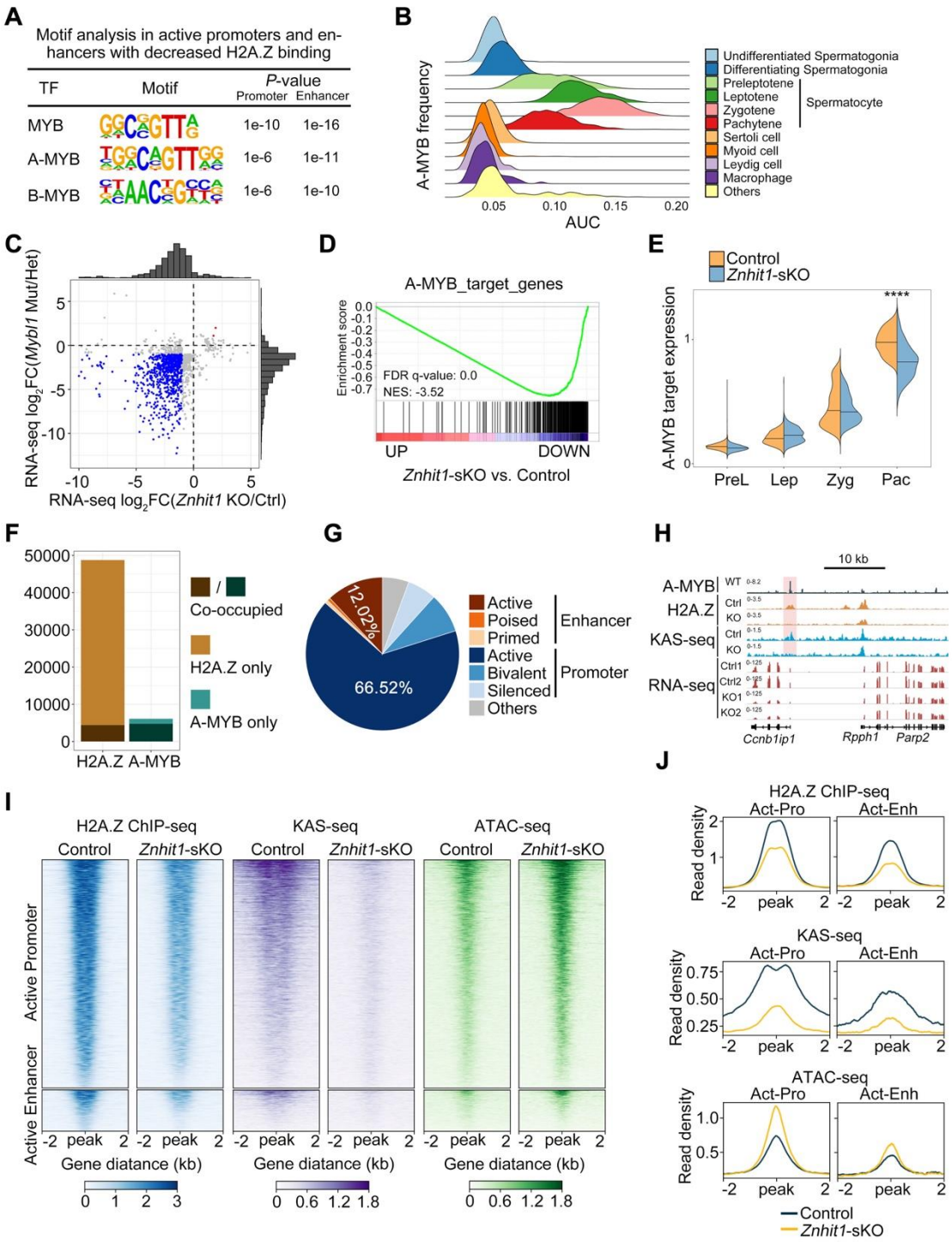

Figure 7 | Znhit1/H2A.Z/A-MYB axis regulates enhancer activation and gene expression. (**A**) Motif analysis of active promoters or active enhancers with decreased H2A.Z binding for putative transcription factor (TF)-binding sites using the HOMER database. (**B**) Ridge map showing the A-MYB activity (AUC) at each cell type. (**C**) Scatter plot with marginal histograms comparing the fold change of DEGs from A-MYB-related RNA-seq data with Znhit1-related RNA-seq data in P14 testicular cells.

(**D**) GSEA of RNA-seq data for the control and *Znhit1*-sKO testicular cells. Selected gene sets encoded products related to A-MYB target genes. (**E**) Violin plots showing the expression of A-MYB target genes at consecutive spermatocyte stages. (**F**) Histogram showing H2A.Z and A-MYB binding sites. (**G**) Pie chart showing the distribution of H2A.Z and A-MYB co-binding sites. (**H**) Representative H2A.Z ChIP-seq tracks, KAS-seq signals, and RNA-seq signals of the *Ccnb1ip1* locus in the control and *Znhit1*-sKO testicular cells, compared with A-MYB ChIP-seq peaks. (**I** and **J**) Heatmaps and mean plots of H2A.Z ChIP-seq, KAS-seq, and ATAC-seq showing signal changes within A-MYB and H2A.Z co-binding active promoters or active enhancers. ******** $p < 0.0001$.

Supplementary Materials for

H2A.Z deposition at meiotic prophase I underlies homologous recombination and pachytene genome activation during male meiosis

Shenfei Sun *et al.*

*Corresponding author. Email: Xinhua Lin, xlin@fudan.edu.cn; Shenfei Sun shenfei_sun@fudan.edu.cn

This PDF file includes:

Figs. S1 to S9

Other Supplementary Material for this manuscript includes the following:

Tables. S1 to S8

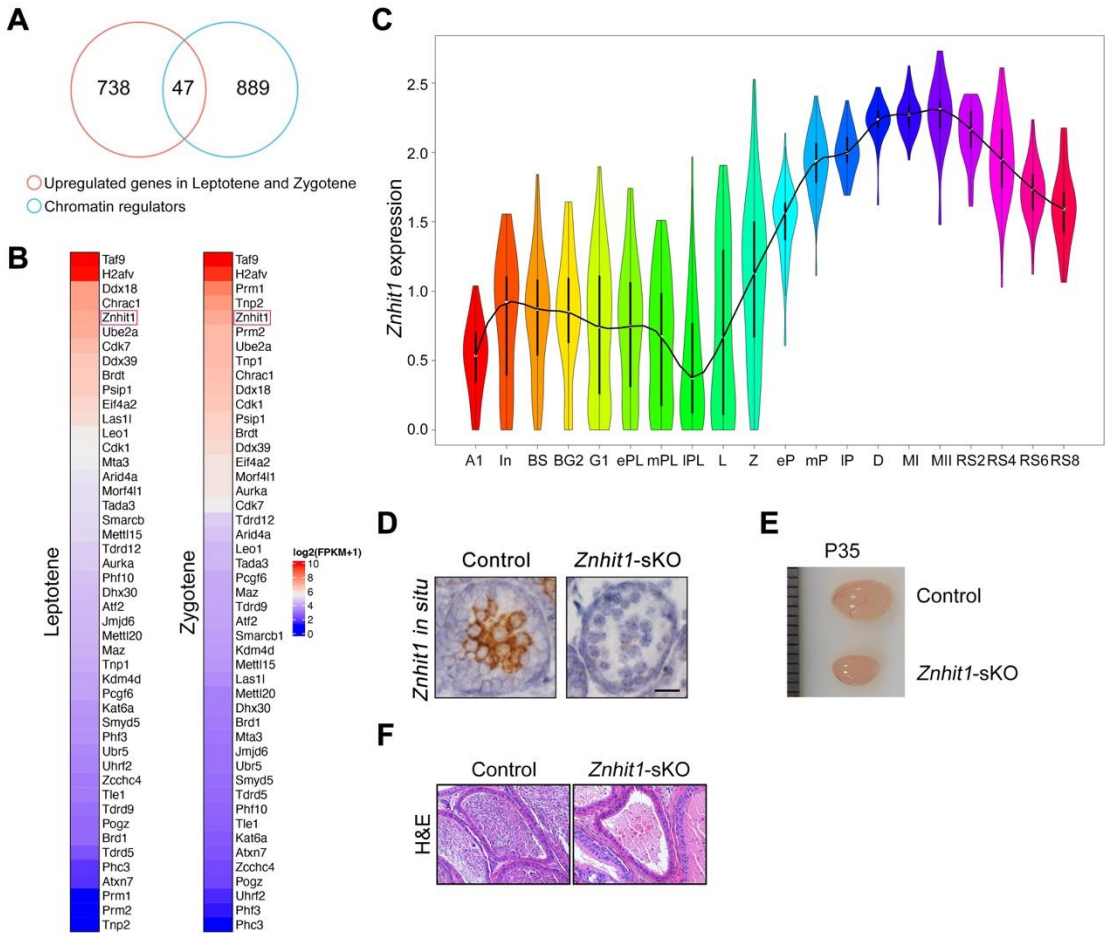

Figure S1. Znhit1 expression during meiotic progression and spermatocyte-specific deletion of Znhit1 with Stra8-cre. (**A** and **B**) Venn diagram and heatmaps showing chromatin regulators highly expressed during leptotene and zygotene spermatocytes. (**C**) Violin plot showing Znhit1 transcription level during spermatogenesis. Gene expression profiles derived from published data (Chen et al, 2018). (**D**) Znhit1 in situ hybridization in P14 testis sections. (**E**) Testis size comparison between control and Znhit1-sKO mice at P35. (**F**) Hematoxylin and eosin (H&E) - stained testis sections from control and Znhit1-sKO mice at P60.

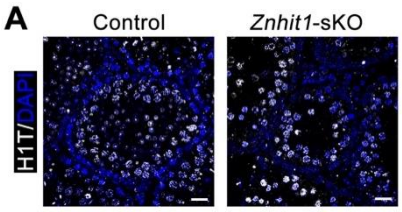

Figure S2. H1T^{+} pachytene spermatocytes are detected in *Znhit1*-sKO testes. (**A**) Immunostaining of H1T in testis sections from control and *Znhit1*-sKO mice at P35. Scale bar, 20 μm.

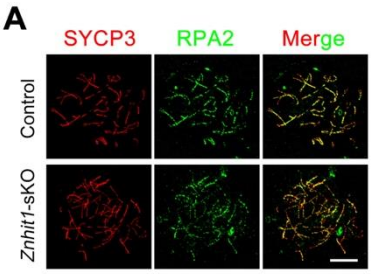

Figure S3. Znhit1 controls meiotic recombination. (**A**) Immunostaining of SYCP3 and RPA2 in spermatocyte chromosome spreads of control or *Znhit1*-sKO mice. Scale bar, 10 μm.

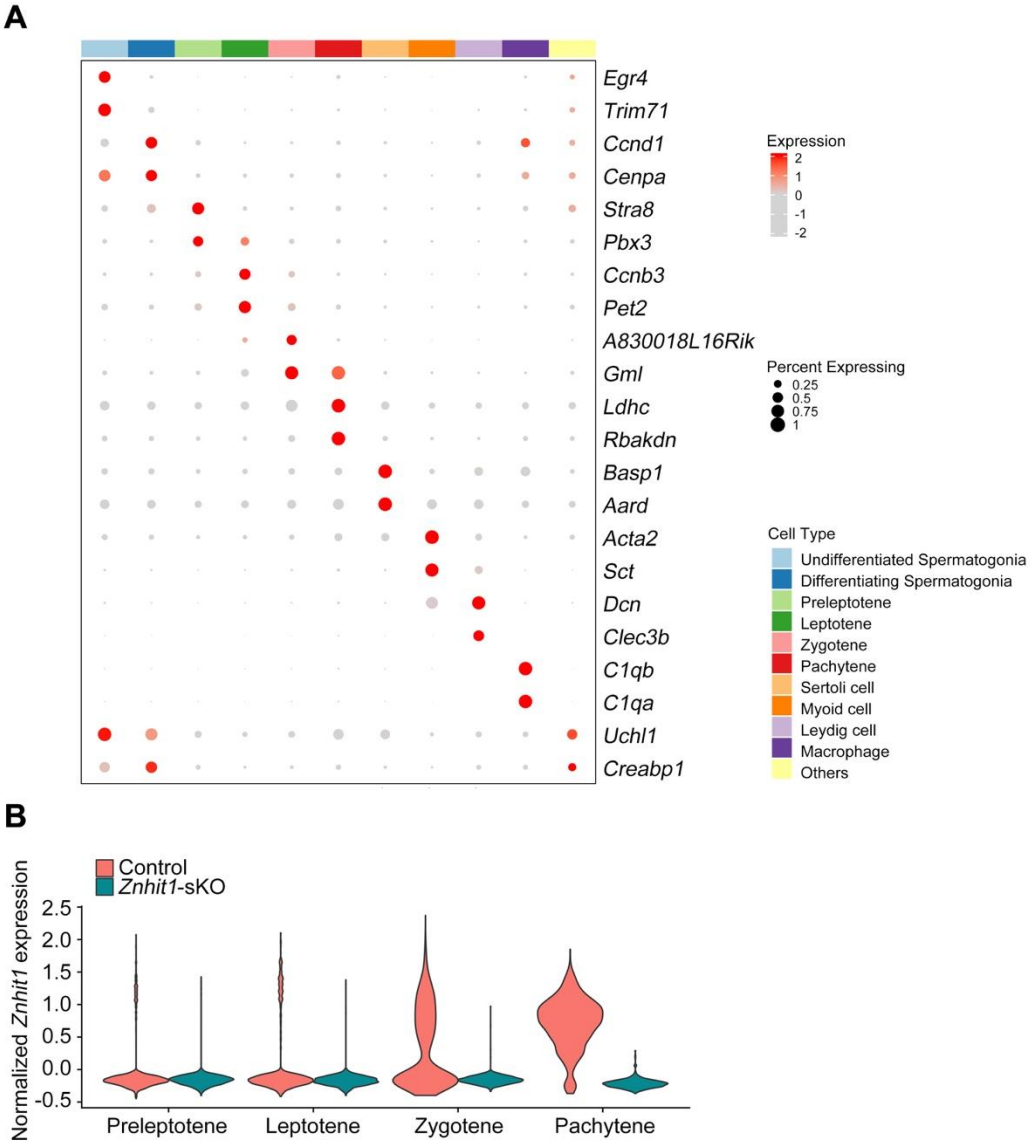

Figure S4. Single-cell RNA-seq of testicular cells. (**A**) Dot plot showing the relative expression and the percentage of cells expressing selected markers across scRNA-seq clusters. (**B**) Violin plot showing the normalized expression of *Znhit1* in control and *Znhit1*-sKO spermatocytes at consecutive stages.

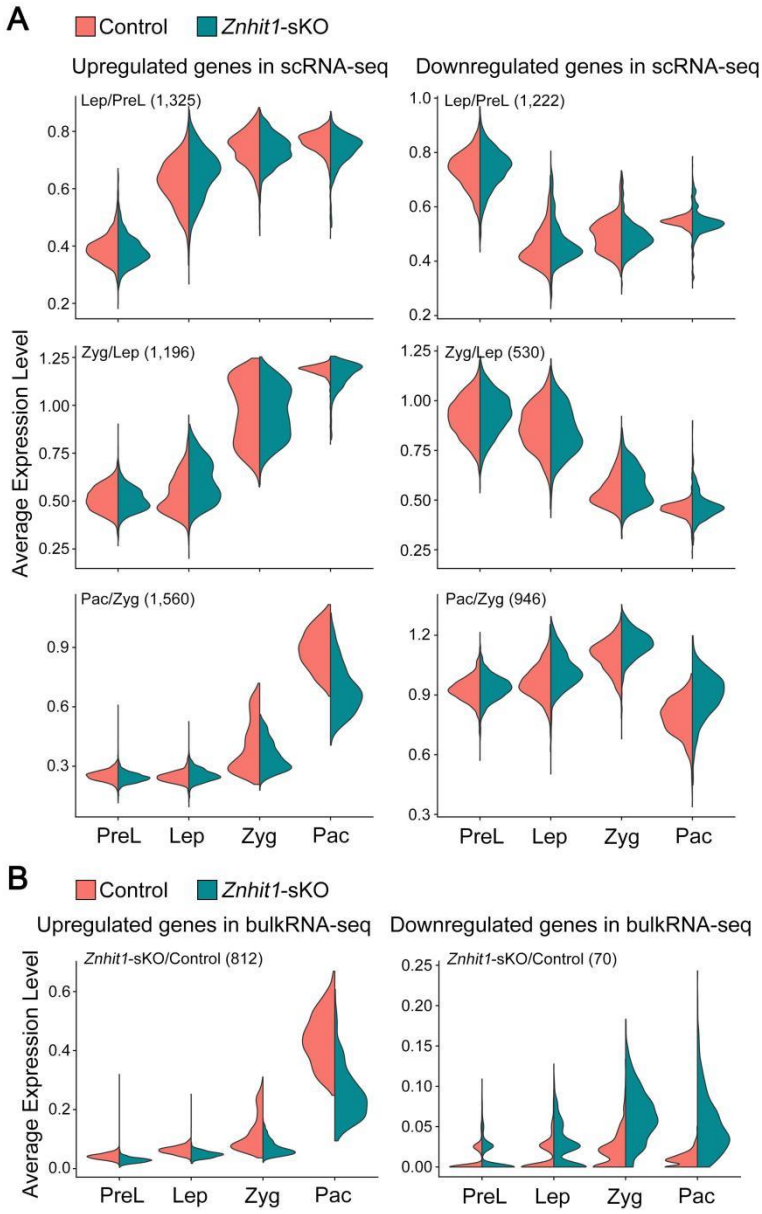

Figure S5. Single-cell transcriptomic analysis of meiotic genome activation. (**A**) Violin plots showing the average expression level of upregulated or downregulated genes between two consecutive spermatocyte stages. (**B**) Violin plots showing the average expression level of upregulated or downregulated genes between P14 control and *Znhit*1-sKO testicular cells. PreL, preleptotene; Lep, leptotene; Zyg, zygotene; Pac, pachytene.

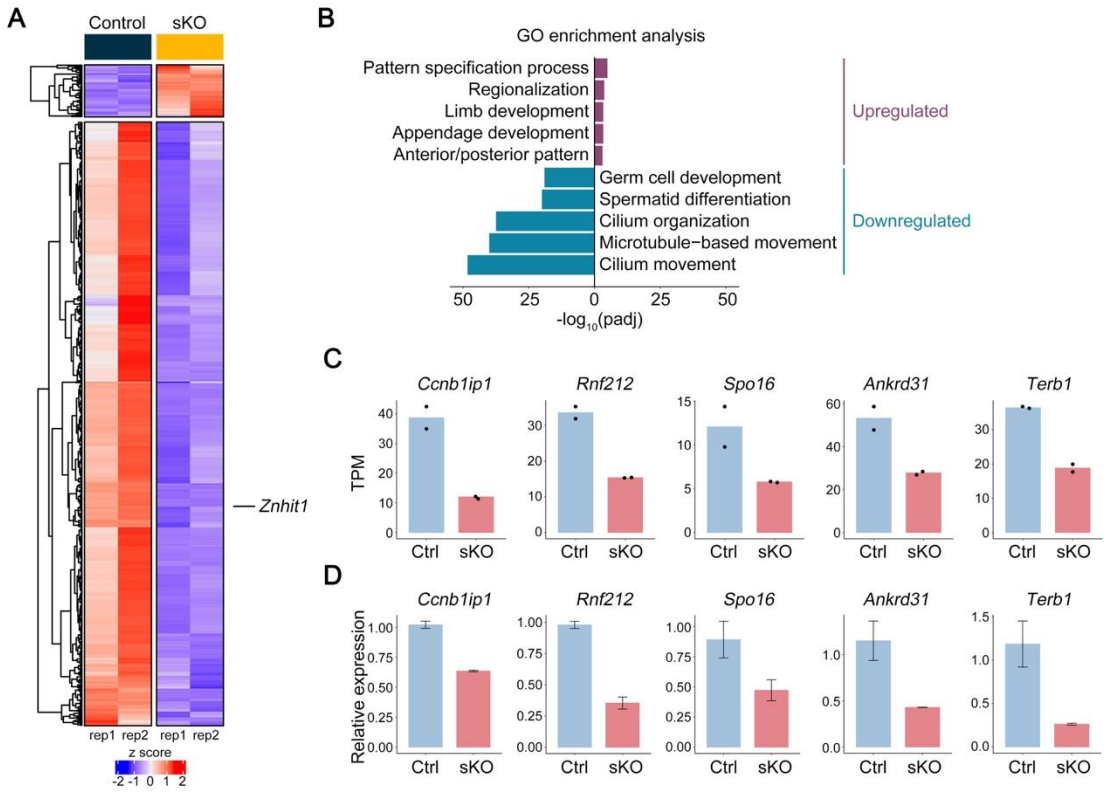

Figure S6. differentially expressed genes (DEGs) in P14 testicular cells between control and Znhit1-sKO mice. (**B**) Gene ontology (GO) analysis of DEGs showing changed biological processes. (**C** and **D**) Bar charts showing HR-related gene expression in P14 control and *Znhit*1-sKO testes. Data from bulk RNA-seq are shown in (**C**). Validated data from RT-qPCR are shown in (**D**). Ctrl, control; sKO, *Znhit1*-sKO.

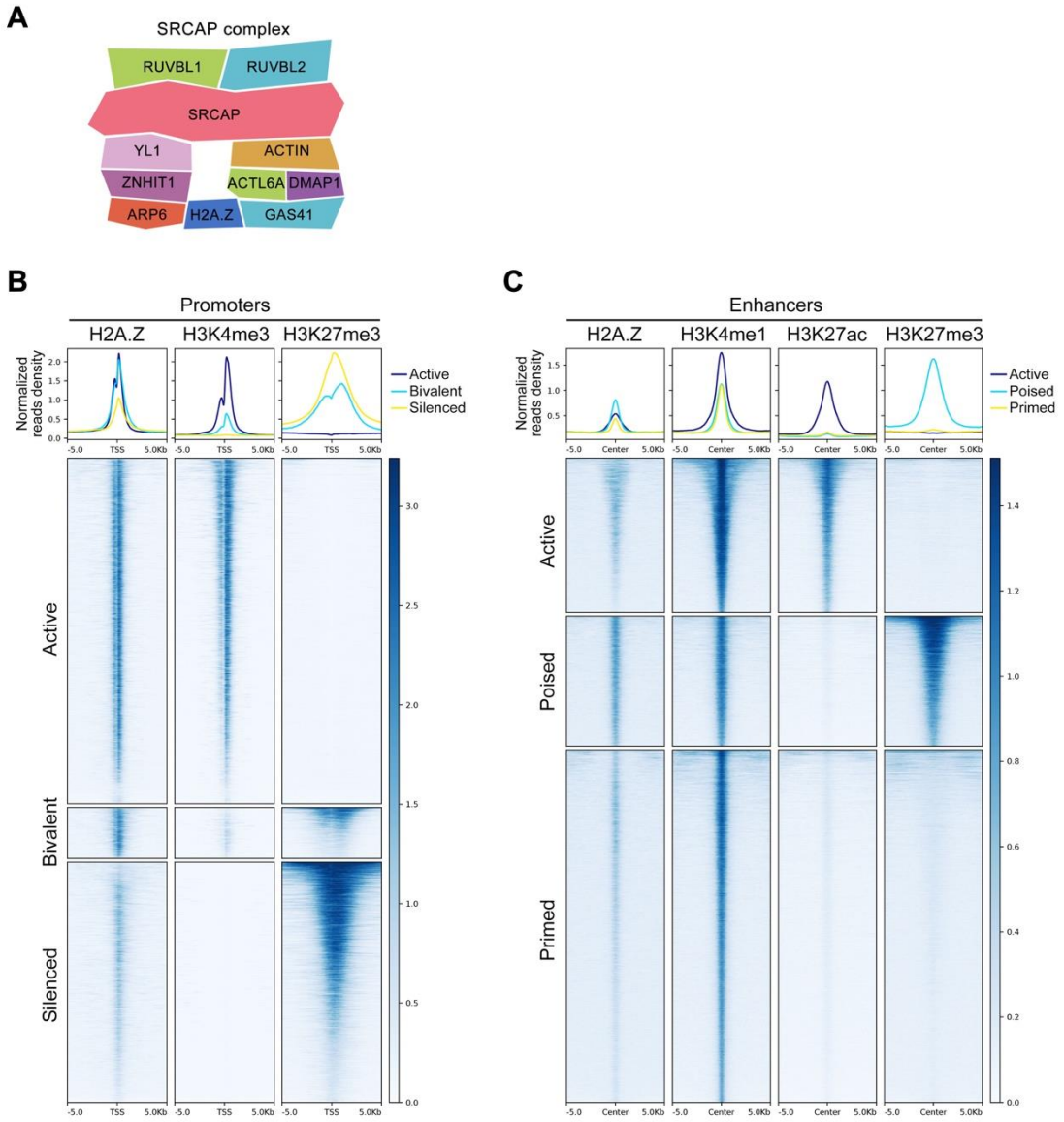

Figure S7. H2A.Z is enriched at meiotic gene promoters and enhancers. (**A**) Schematic representation of the components of the SRCAP chromatin remodeling complex. (**B**) Heatmaps showing H2A.Z ChIP-seq signals surrounding different types of promoters. (**C**) Heatmaps showing H2A.Z ChIP-seq signals surrounding different types of enhancers.

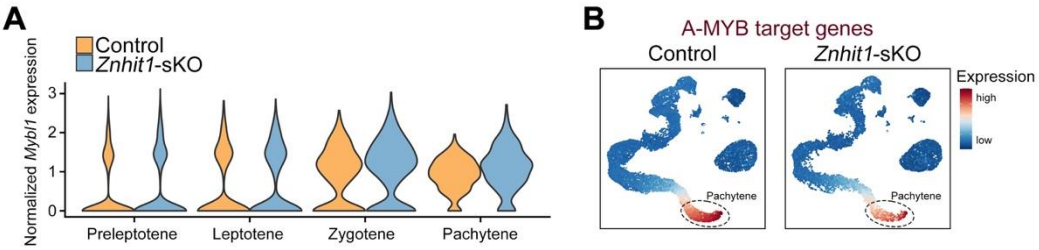

Figure S8. Znhit1 deletion downregulates the expression of A-MYB target genes. (**A**) Violin plot showing the normalized expression of *Mybl1* in control and *Znhit1*-sKO spermatocytes at consecutive stages. (B) Cluster annotation on the basis of the expression of A-MYB target genes in control or *Znhit1*-sKO testicular cells.

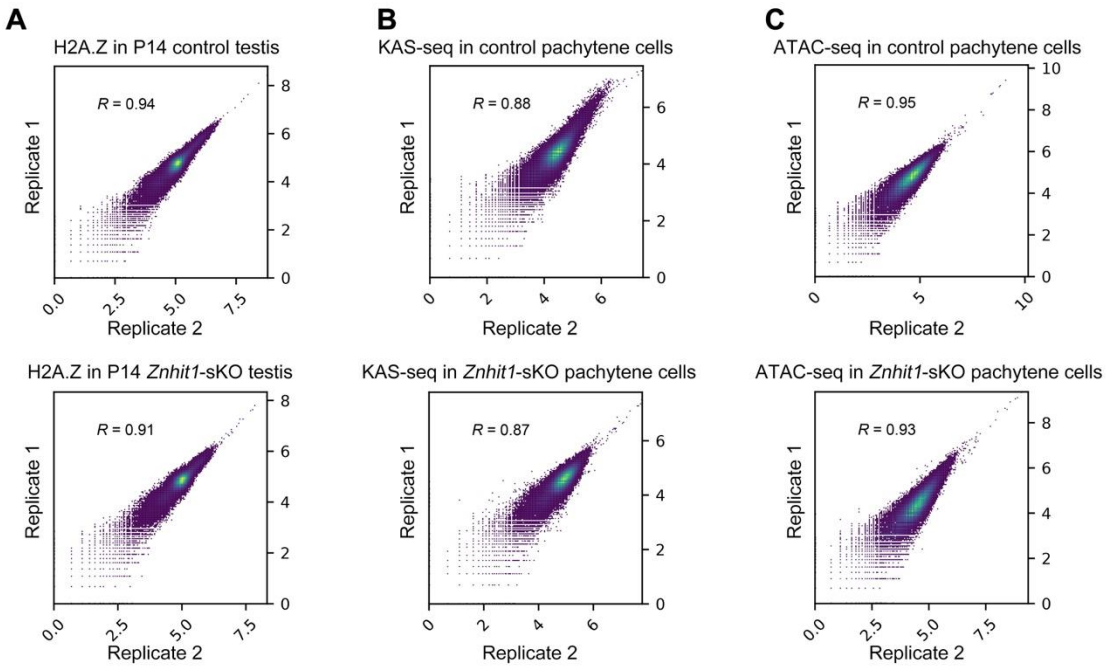

Figure S9. Reproducibility of replicates in this study. (**A**) Scatter plots showing H2A.Z enrichments in P14 control or *Znhit1*-sKO testes for two independent H2A.Z ChIP-seq replicates. Pearson correlation coefficients are indicated. (**B**) Scatter plots showing KAS-seq signals in P14 control or *Znhit1*-sKO pachytene cells for two independent H2A.Z ChIP-seq replicates. Pearson correlation coefficients are indicated. (**C**) Scatter plots showing ATAC-seq signals in P14 control or *Znhit1*-sKO pachytene cells for two independent H2A.Z ChIP-seq replicates. Pearson correlation coefficients are indicated.